Supporting Information for "AFRP20: New P-wavespeed Model for the African Mantle Reveals Two Whole-Mantle Plumes Below East Africa and Neoproterozoic Modification of the Tanzania Craton"

A. Boyce[1,2*], I. D. Bastow[1], S. Cottaar[2], R. Kounoudis[1], J. Guilloud De Courbeville[1], E. Caunt[1], S. Desai[1]

[1]Department of Earth Science and Engineering, Royal School of Mines, Prince Consort Road, Imperial College London, London, SW7 2BP, UK.
[2]University of Cambridge, Department of Earth Science, Bullard Laboratories, Madingley Road, Cambridge, CB3 0EZ, UK.

[*]Present Address : University of Cambridge, Department of Earth Science, Bullard Laboratories, Madingley Road, Cambridge, CB3 0EZ, UK.

Corresponding author: Alistair Boyce, ab2568@cam.ac.uk

Contents of this file

1 Introduction

A digital model file of the AFRP20 tomographic model with and without the crustal correction will be made available through http://ds.iris.edu/ds/products/emc/ or by contacting the corresponding author (email: ab2568@cam.ac.uk). Also available is ray path mask described in Section 12. The python code used to compute this mask is available at https://github.com/alistairboyce11/Ray_path_mask.

2 The Global Data set

Figures S1 and S2 show the earthquake and station locations used in the tomographic inversion. Phase arrivals from the EHB Bulletin are available at http://www.isc.ac.uk/ehbbulletin/. We make use of further phase arrivals used by Burdick et al. (2017) and Boyce et al. (2019) to more accurately constrain the background model.

3 Direct P-wave Absolute Arrival-time Residuals

Figure S3 shows the direct-P phase mean absolute arrival-time residuals for stations in the "EHB" database (Engdahl et al., 1998) used by Li et al. (2008), along with those from African data sets added here (see main manuscript). Residuals from other phases (e.g., Pn, Pg, pP, PKP and PKIKP) are not plotted but are used to better constrain the crust and deep mantle.

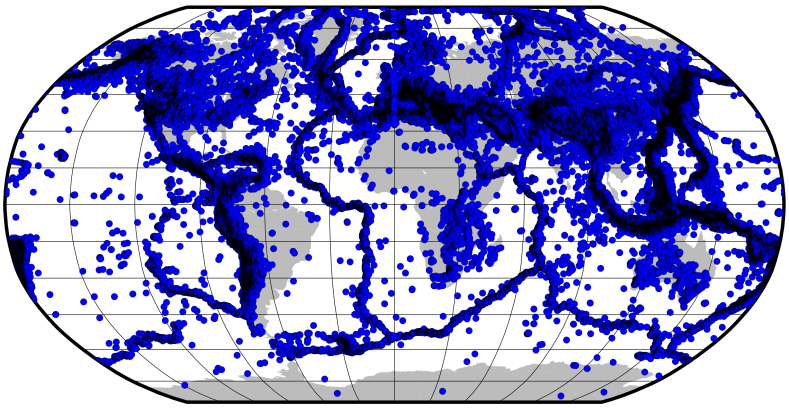

Figure S1. Earthquake map derived from the EHB Bulletin (see Li et al., 2008) and supplementary data used by Burdick et al. (2017) and Boyce et al. (2019), combined with teleseismic earthquakes recorded across Africa.

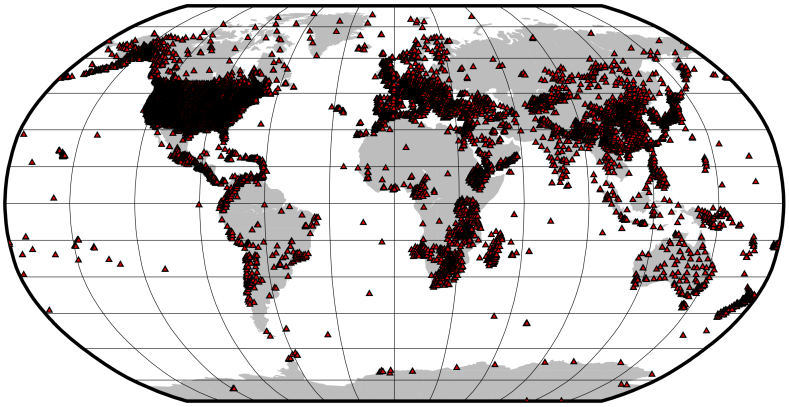

Figure S2. Seismograph station map derived from the EHB Bulletin (see Li et al., 2008) and supplementary data used by Burdick et al. (2017) and Boyce et al. (2019), combined with the publicly available networks across Africa used here.

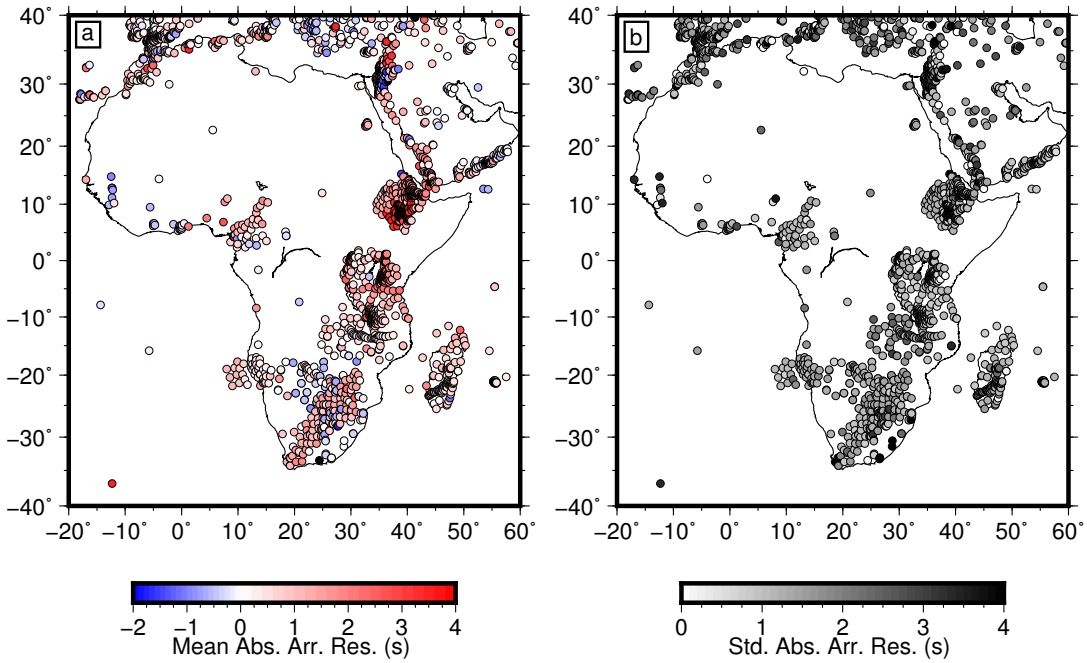

Figure S3. Mean *(a)* and standard deviation *(b)* of the direct-P phase absolute arrival-time residuals for the "EHB" database (Engdahl et al., 1998) used by Li et al. (2008) and African data summarized in the main manuscript (Figure 2). African stations within the "EHB" database contribute 182,853 direct P-wave arrival-times while our African data contributes 87,184 arrival-times.

4 Relative Arrival-time Analysis

Vertical component broadband seismic data was collected from all publicly available seismograph stations across Africa for m_b >5.5 earthquakes with high SNR for the period 1990–2019. These networks were split into 6 regions, namely; Atlas Mountains, Cameroon, Ethiopia, East Africa, Madagascar and Southern Africa (Figure S4). Relative arrival-time residuals were obtained from these networks separately using Multi-Channel Cross-correlation (VanDecar & Crosson, 1990). The exact processing steps are outlined in Boyce et al. (2016). For the Atlas Mountains we obtain 16,161 picks from 697 earthquakes recorded at 122 stations. For Cameroon we obtain 3,810 picks from 409 earthquakes recorded at 44 stations. For Ethiopia we obtain 32,091 picks from 1,693 earthquakes recorded at 427 stations. For the East African rift we obtain 26,904 picks from 1,337 earthquakes recorded at 333 stations. For Madagascar we obtain 8,379 picks from 398 earthquakes recorded at 128 stations. For Southern Africa we obtain 15,400 picks from 1,114 earthquakes recorded at 221 stations. These results are presented in Figures S5-S10.

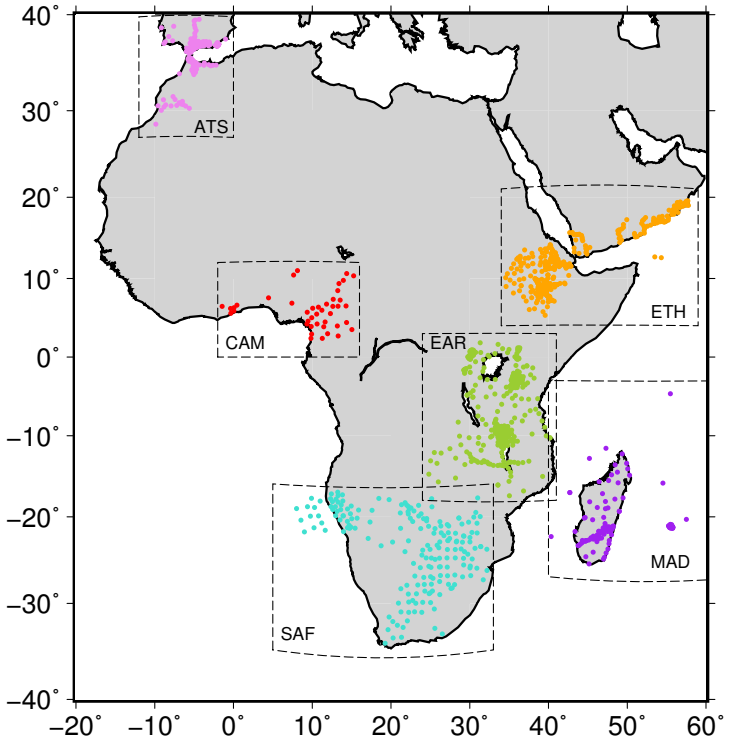

Figure S4. Map of publicly available seismic stations across Africa initially processed separately (Figures S5–S10), colored by sub region. ATS: Atlas Mountains, CAM: Cameroon, ETH: Ethiopia, EAR: East Africa, MAD: Madagascar, SAF: Southern Africa.

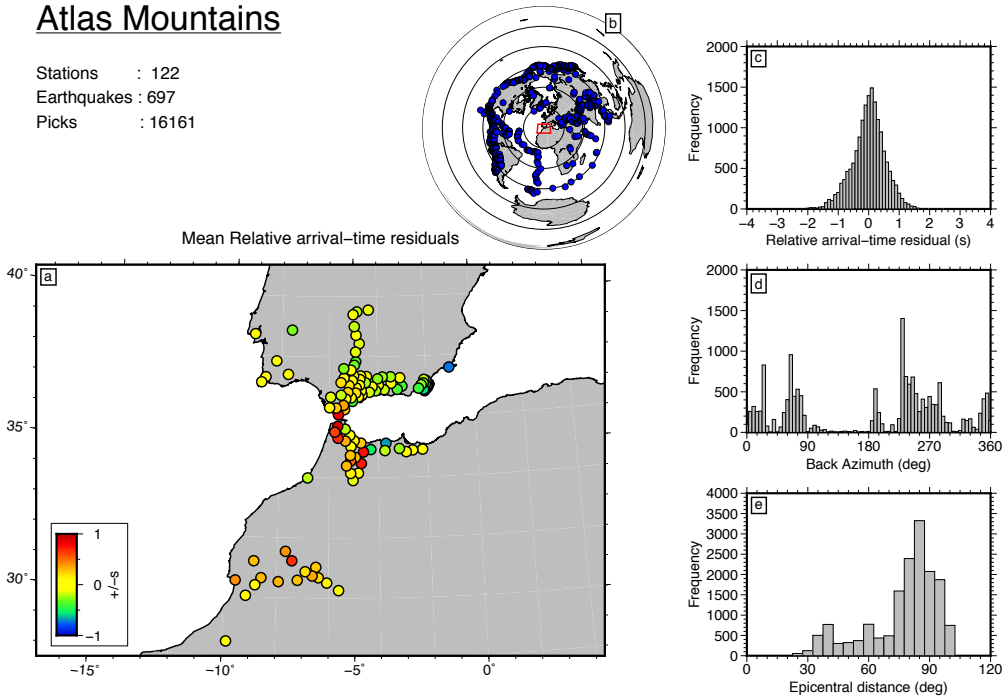

Figure S5. For the Atlas Mountains data set: (*a*) Regional map showing the mean relative arrival-time residual for each station calculated using Multi-channel cross-correlation after VanDecar and Crosson (1990). (*b*) Teleseismic earthquakes of magnitude m_b >5.5 contributing to the data set shown as blue dots. These earthquakes are recorded with adequate SNR at ≥ 4 stations across the regional network. Concentric rings are separated by 30° increments in epicentral distance from the centre of the network. (*c*) Distribution of relative arrival-time residuals. (*d*) Residual distribution with back-azimuth. (*e*) Residual distribution with epicentral distance.

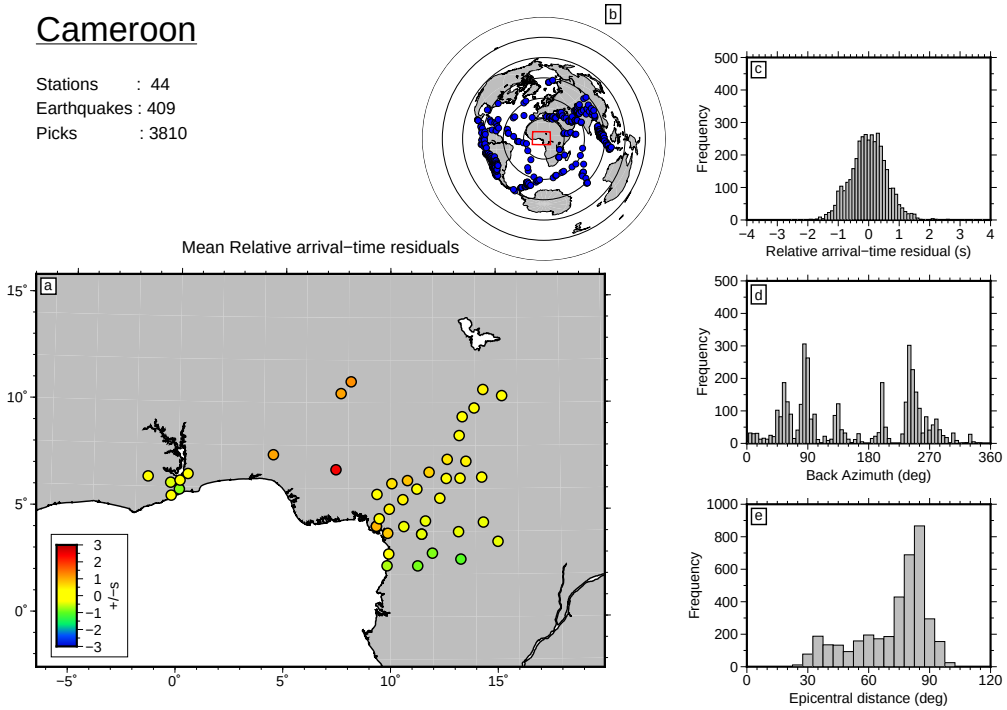

Figure S6. For the Cameroon data set: (*a*) Regional map showing the mean relative arrival-time residual for each station calculated using Multi-channel cross-correlation after VanDecar and Crosson (1990). (*b*) Teleseismic earthquakes of magnitude m_b >5.5 contributing to the data set shown as blue dots. These earthquakes are recorded with adequate SNR at ≥ 4 stations across the regional network. Concentric rings are separated by 30° increments in epicentral distance from the centre of the network. (*c*) Distribution of relative arrival-time residuals. (*d*) Residual distribution with back-azimuth. (*e*) Residual distribution with epicentral distance.

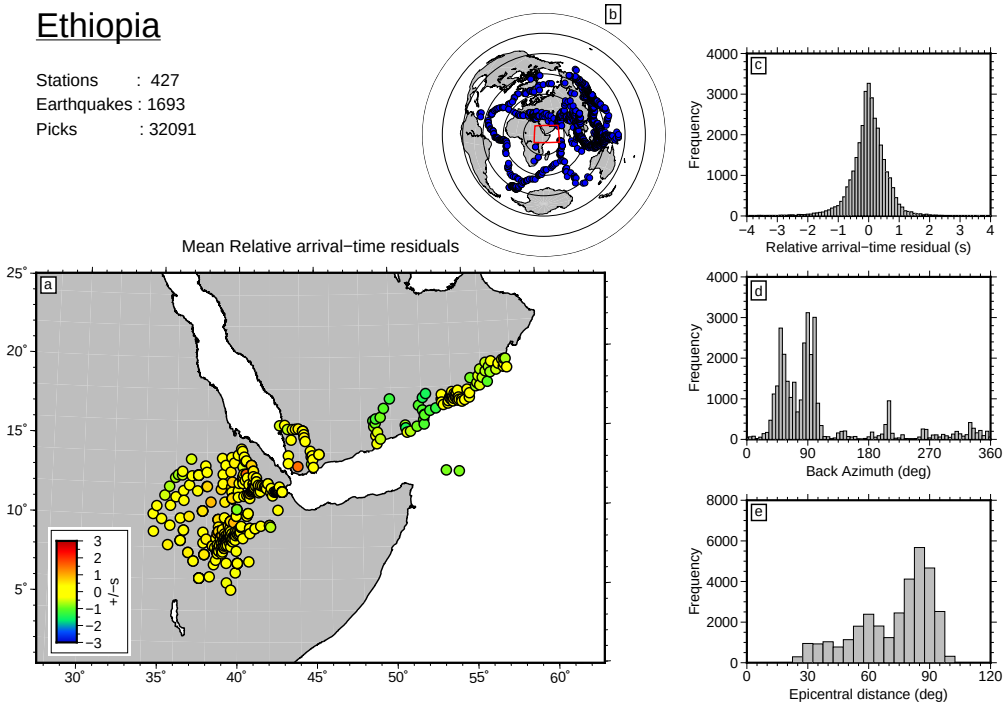

Figure S7. For the Ethiopia data set: (*a*) Regional map showing the mean relative arrival-time residual for each station calculated using Multi-channel cross-correlation after VanDecar and Crosson (1990). (*b*) Teleseismic earthquakes of magnitude m_b >5.5 contributing to the data set shown as blue dots. These earthquakes are recorded with adequate SNR at ≥ 4 stations across the regional network. Concentric rings are separated by 30° increments in epicentral distance from the centre of the network. (*c*) Distribution of relative arrival-time residuals. (*d*) Residual distribution with back-azimuth. (*e*) Residual distribution with epicentral distance.

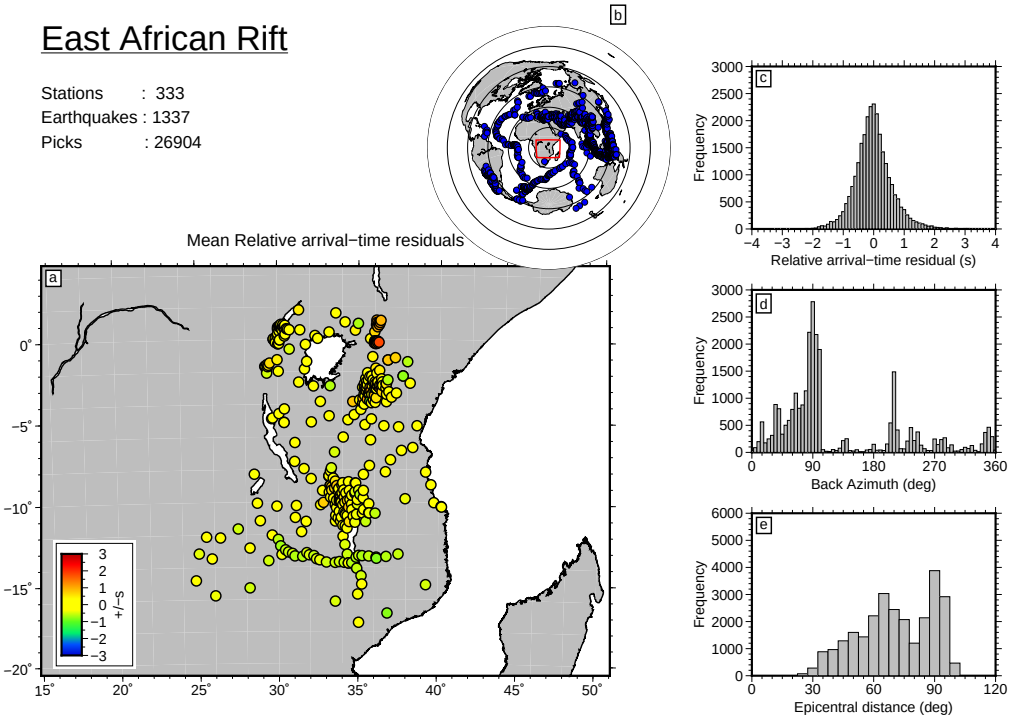

Figure S8. For the East Africa data set: (*a*) Regional map showing the mean relative arrival-time residual for each station calculated using Multi-channel cross-correlation after VanDecar and Crosson (1990). (*b*) Teleseismic earthquakes of magnitude m_b >5.5 contributing to the data set shown as blue dots. These earthquakes are recorded with adequate SNR at ≥ 4 stations across the regional network. Concentric rings are separated by 30° increments in epicentral distance from the centre of the network. (*c*) Distribution of relative arrival-time residuals. (*d*) Residual distribution with back-azimuth. (*e*) Residual distribution with epicentral distance.

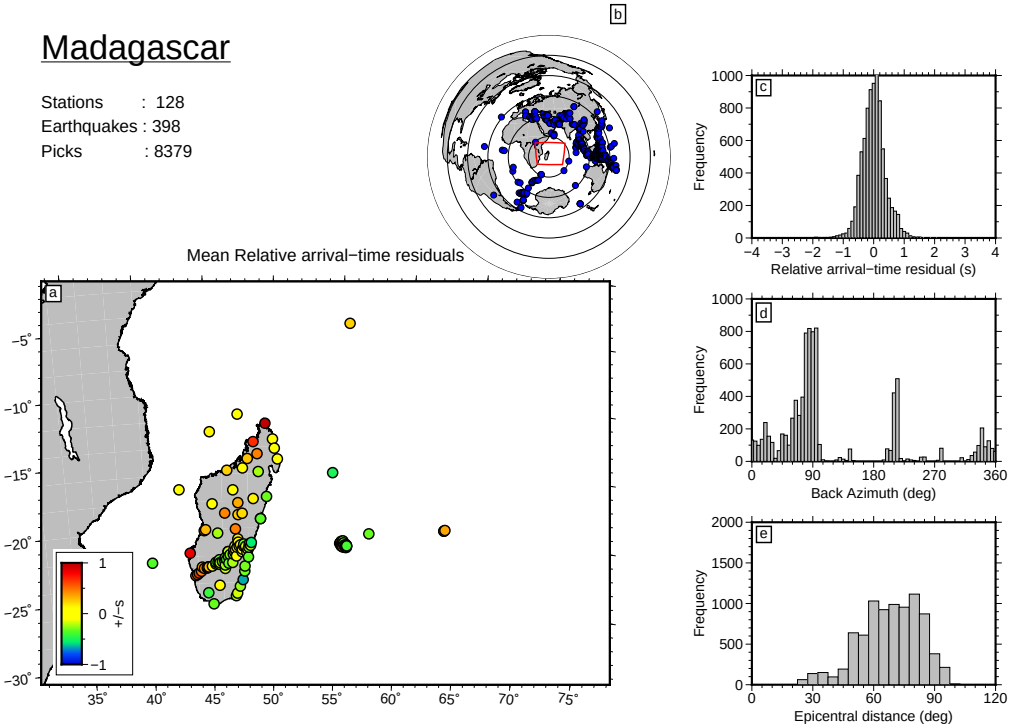

Figure S9. For the Madagascar data set: (*a*) Regional map showing the mean relative arrival-time residual for each station calculated using Multi-channel cross-correlation after VanDecar and Crosson (1990). (*b*) Teleseismic earthquakes of magnitude m_b >5.5 contributing to the data set shown as blue dots. These earthquakes are recorded with adequate SNR at ≥ 4 stations across the regional network. Concentric rings are separated by 30° increments in epicentral distance from the centre of the network. (*c*) Distribution of relative arrival-time residuals. (*d*) Residual distribution with back-azimuth. (*e*) Residual distribution with epicentral distance.

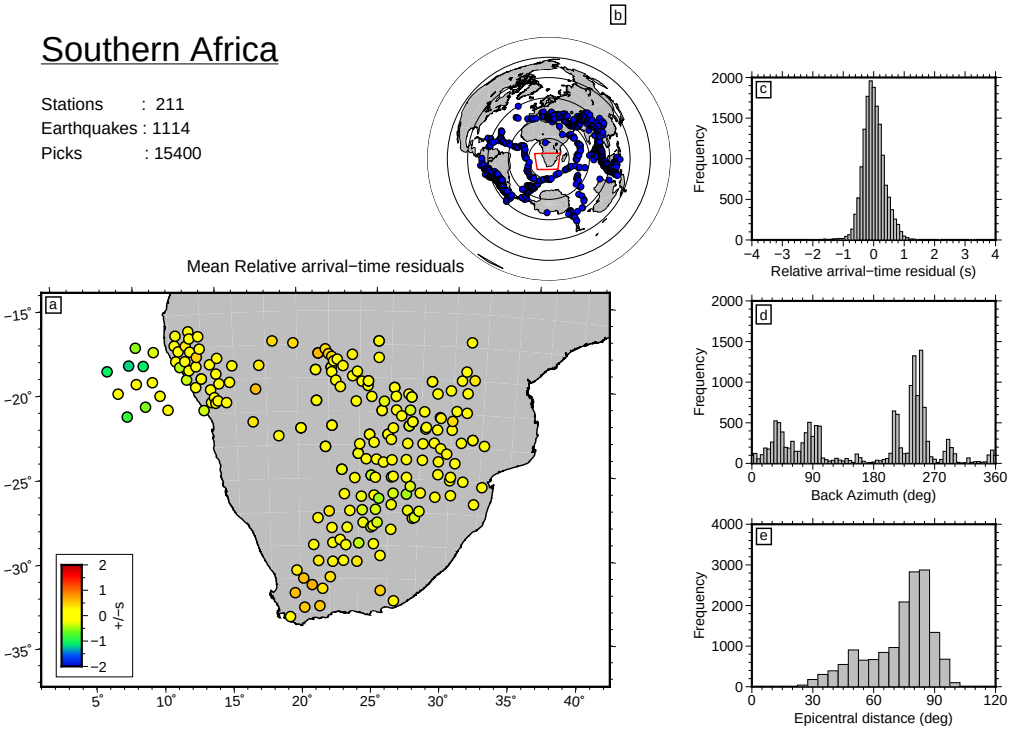

Figure S10. For the Southern Africa data set: (*a*) Regional map showing the mean relative arrival-time residual for each station calculated using Multi-channel cross-correlation after VanDecar and Crosson (1990). (*b*) Teleseismic earthquakes of magnitude m_b >5.5 contributing to the data set shown as blue dots. These earthquakes are recorded with adequate SNR at ≥ 4 stations across the regional network. Concentric rings are separated by 30° increments in epicentral distance from the centre of the network. (*c*) Distribution of relative arrival-time residuals. (*d*) Residual distribution with back-azimuth. (*e*) Residual distribution with epicentral distance.

5 Absolute Arrival-time Analysis

Relative arrival-times derived from regional seismic networks can be processed using the Absolute Arrival-time Recovery Method (AARM - see Boyce et al., 2017) to yield absolute travel-times, comparable with global pick databases. Processing using AARM produced 14,385 absolute travel-time picks for the Atlas Mountains, 3,117 for Cameroon, 27,641 for Ethiopia, 22,264 for the East African Rift, 6,760 for Madagascar and 12,997 for Southern Africa (Figures S11-S16).

6 Adaptive Parameterization

The adaptively parameterized grid of cells within the inversion is displayed at four depths (*a*–*d*: 100–660 km) in Figure S17. Cells are plotted as fine black lines over the AFRP20 tomographic model, with respective anomalies plotted as in the main manuscript.

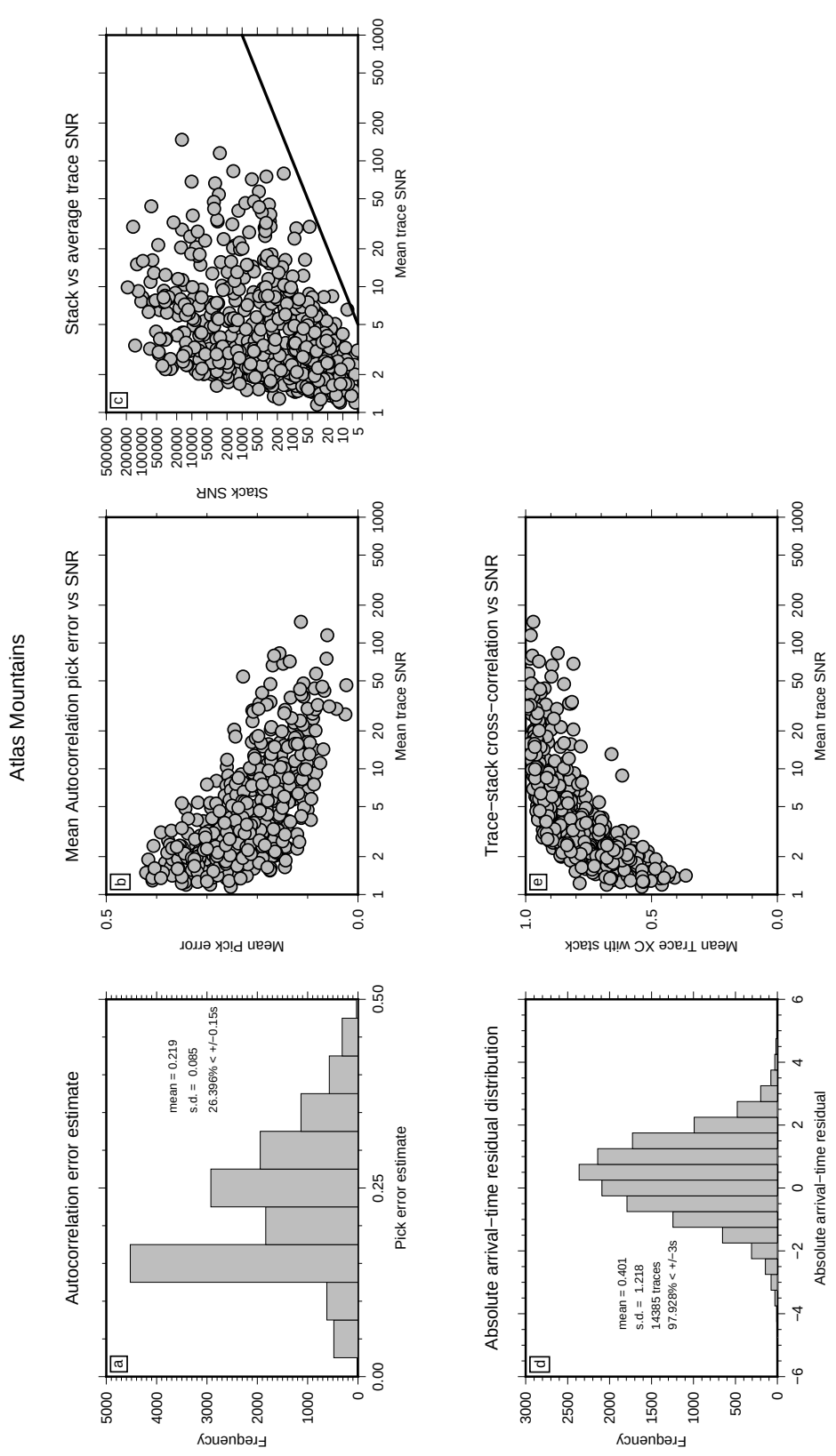

Figure S11. For the Atlas Mountains data set: (*a*) Distribution of autocorrelation pick error estimates for each arrival-time. (*b*) Mean autocorrelation pick error against mean trace SNR for each earthquake. (*c*) Stacked trace SNR against mean trace SNR for each earthquake. The black line shows the line y=x. (*d*) Distribution of absolute arrival-time residuals. (*e*) Mean cross-correlation coefficient of each trace with the stack against mean trace SNR for each earthquake.

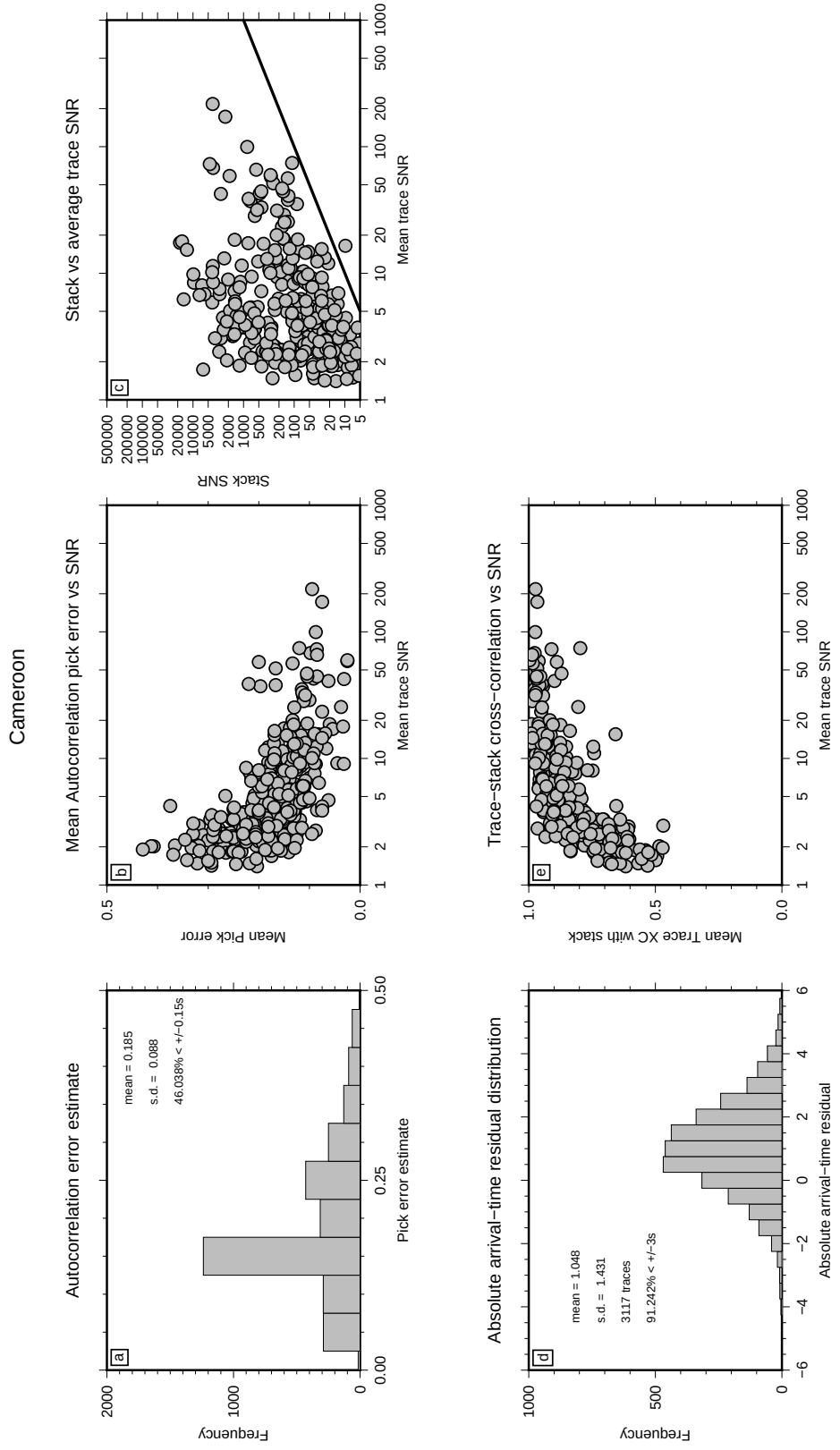

Figure S12. For the Cameroon data set: (*a*) Distribution of autocorrelation pick error estimates for each arrival-time. (*b*) Mean autocorrelation pick error against mean trace SNR for each earthquake. (*c*) Stacked trace SNR against mean trace SNR for each earthquake. The black line shows the line y=x. (*d*) Distribution of absolute arrival-time residuals. (*e*) Mean cross-correlation coefficient of each trace with the stack against mean trace SNR for each earthquake.

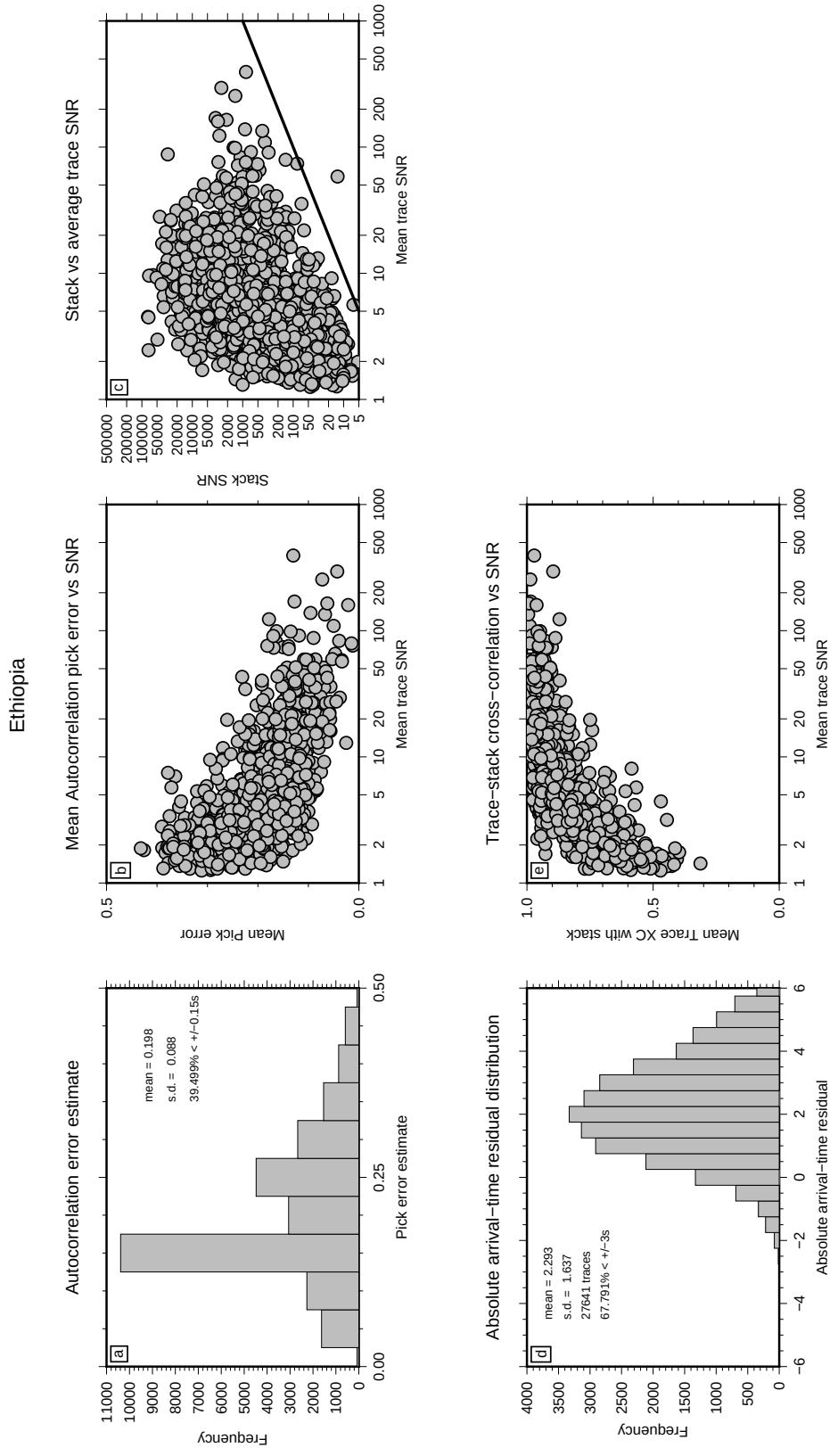

Figure S13. For the Ethiopian data set: (*a*) Distribution of autocorrelation pick error estimates for each arrival-time. (*b*) Mean autocorrelation pick error against mean trace SNR for each earthquake. (*c*) Stacked trace SNR against mean trace SNR for each earthquake. The black line shows the line y=x. (*d*) Distribution of absolute arrival-time residuals. (*e*) Mean cross-correlation coefficient of each trace with the stack against mean trace SNR for each earthquake.

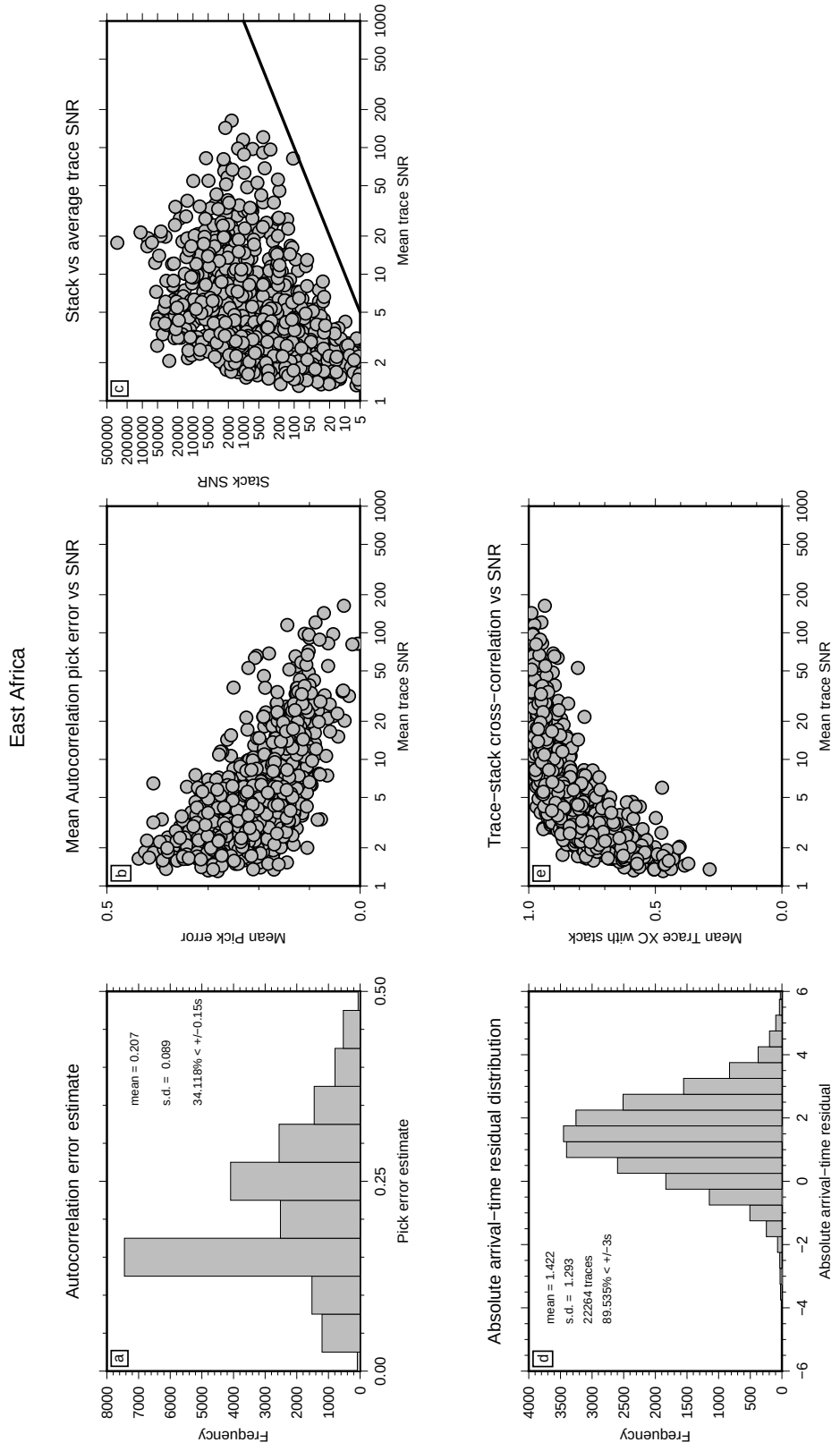

Figure S14. For the East Africa data set: (*a*) Distribution of autocorrelation pick error estimates for each arrival-time. (*b*) Mean autocorrelation pick error against mean trace SNR for each earthquake. (*c*) Stacked trace SNR against mean trace SNR for each earthquake. The black line shows the line y=x. (*d*) Distribution of absolute arrival-time residuals. (*e*) Mean cross-correlation coefficient of each trace with the stack against mean trace SNR for each earthquake.

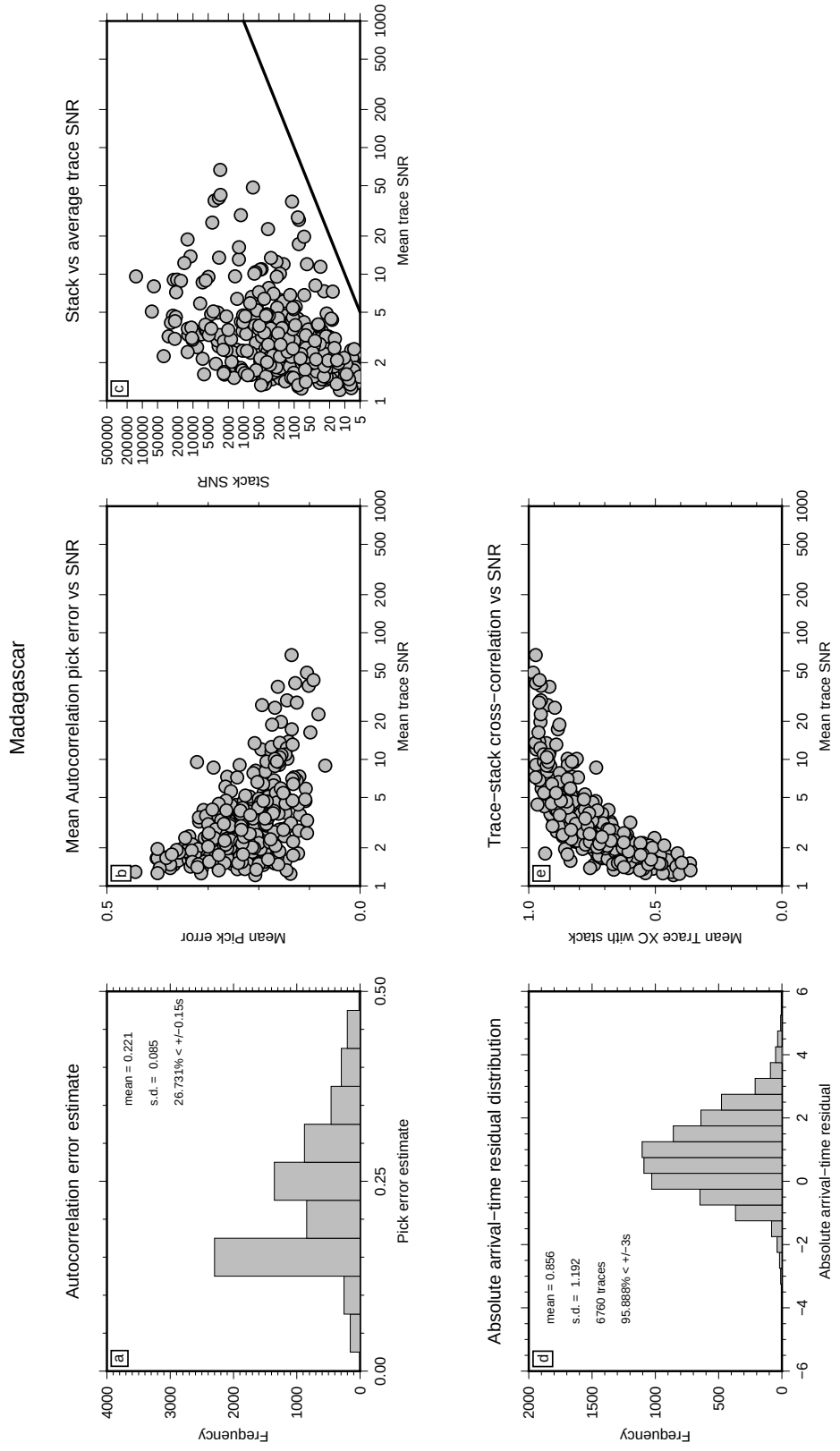

Figure S15. For the Madagascar data set: (*a*) Distribution of autocorrelation pick error estimates for each arrival-time. (*b*) Mean autocorrelation pick error against mean trace SNR for each earthquake. (*c*) Stacked trace SNR against mean trace SNR for each earthquake. The black line shows the line y=x. (*d*) Distribution of absolute arrival-time residuals. (*e*) Mean cross-correlation coefficient of each trace with the stack against mean trace SNR for each earthquake.

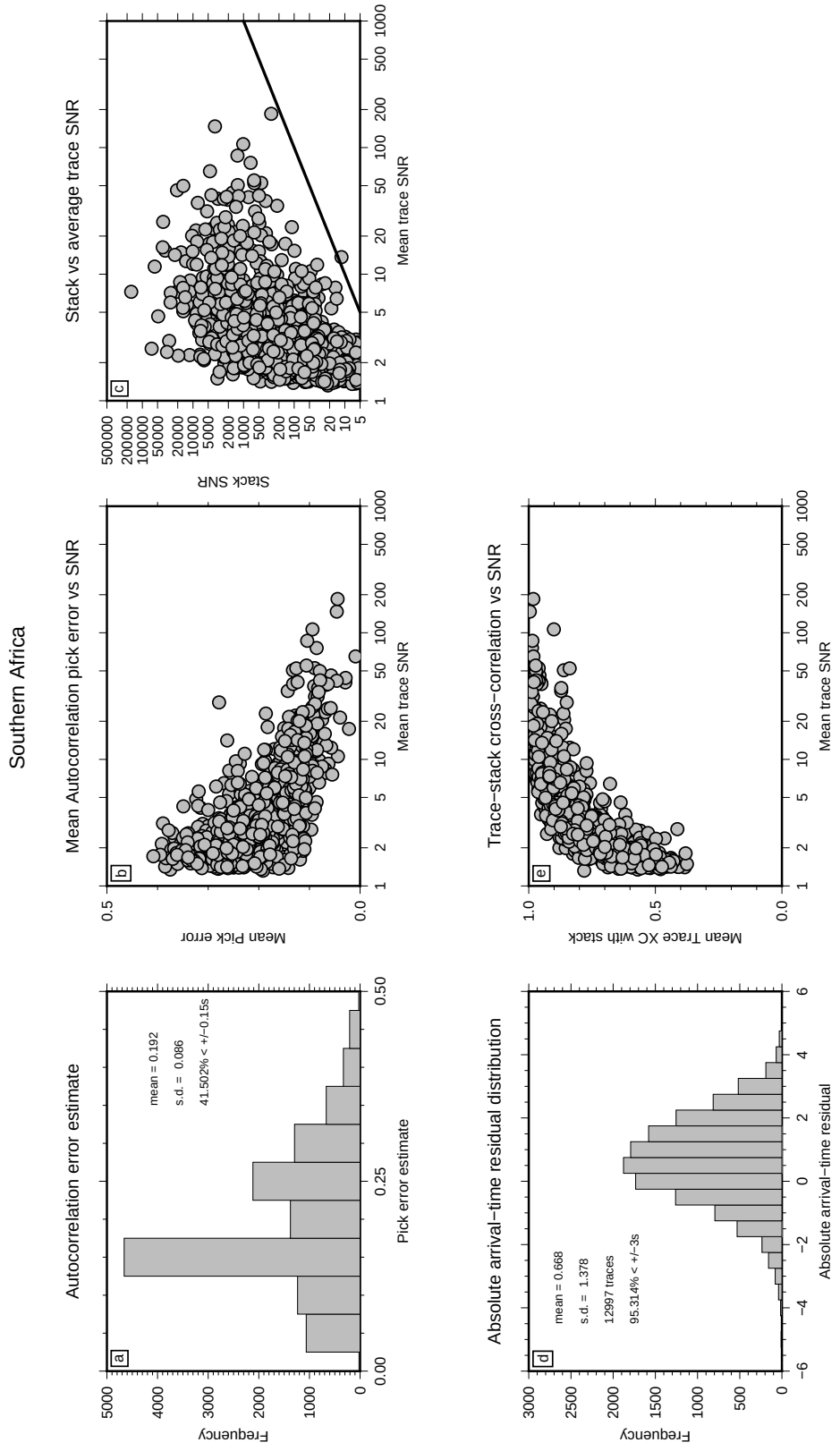

Figure S16. For the Southern Africa data set: (*a*) Distribution of autocorrelation pick error estimates for each arrival-time. (*b*) Mean autocorrelation pick error against mean trace SNR for each earthquake. (*c*) Stacked trace SNR against mean trace SNR for each earthquake. The black line shows the line y=x. (*d*) Distribution of absolute arrival-time residuals. (*e*) Mean cross-correlation coefficient of each trace with the stack against mean trace SNR for each earthquake.

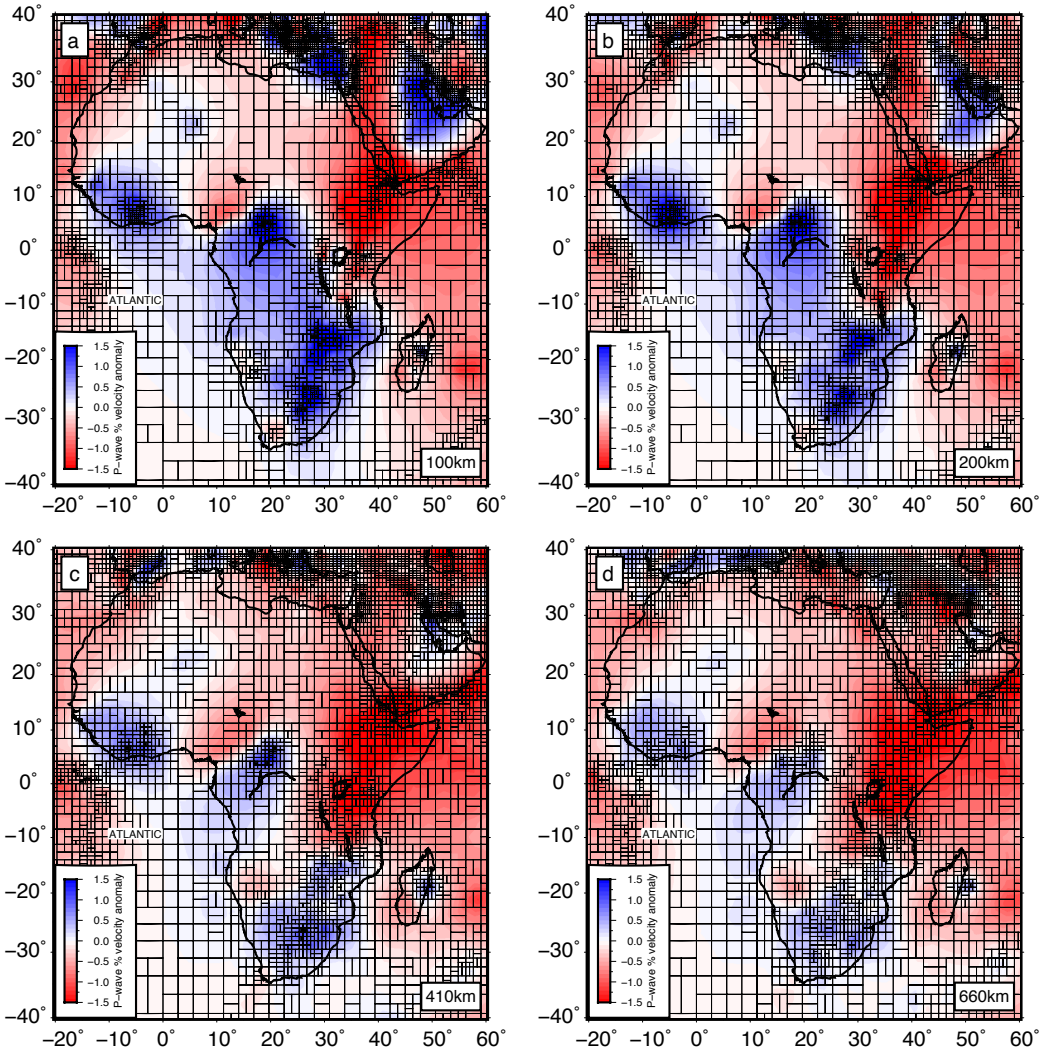

Figure S17. At four depths (*a*–*d*: 100–660 km), fine black cells indicate the adaptively parameterized grid used in the inversion for AFRP20 tomographic model. Wavespeed anomalies are plotted as percentage deviation from ak135 (δV_P=±1.5%).

7 Trade-off Curve Approach

The trade-off curves used to determine the vertical- and horizontal-gradient smoothing parameters in AFRP20 is shown in Figure S18. Our selected model "E" lies close to the knee of both curves in the global parameterization. Model damping is selected following a similar procedure.

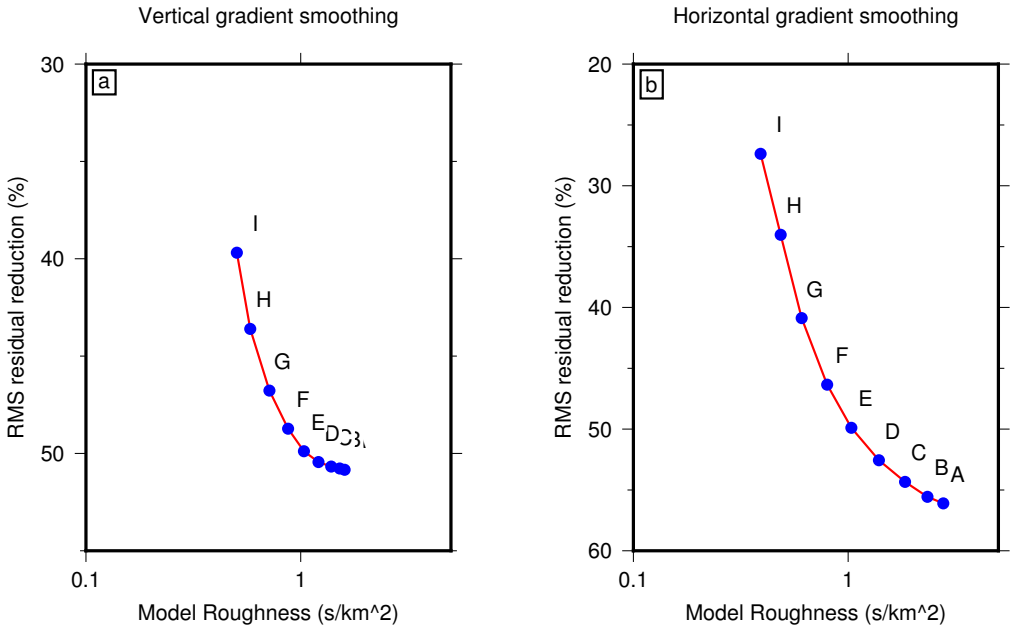

Figure S18. (*a*) vertical- and (*b*) horizontal-gradient smoothing parameters used in the inversion for AFRP20 are determined through a trade-off curve approach. Root-mean-squared residual reduction (%) is plotted against model roughness (s/km^2). We choose model "E" which results in a RMS residual reduction of 49.8%.

8 Bespoke Crustal Model

We use a crustal Moho depth model to correct our absolute arrival-time residual data prior to inversion. By removing the estimated contribution of the crust from each residual we only invert for wavespeed structure resulting from mantle wavespeed anomalies. We compile receiver function (RF) Moho depth estimates across Africa from Akpan et al. (2016); Hosny and Nyblade (2016); Andriampenomanana et al. (2017); Ebinger et al. (2017); Lemnifi et al. (2017); Fadel et al. (2018); Ogden et al. (2019) and use these to improve the Moho depth within Crust1.0 (Laske et al., 2013), because Moho depth imparts the strongest control on the effect of crustal models within tomographic inversions. These Moho depth estimates are derived from station networks across seven regions in the Atlas Mountains, Cameroon, Northern Africa, Ethiopia, East Africa, Madagascar and Southern Africa.

First we interpolate the RF Moho depth estimates between points within each region of stations. We also smooth CRUST1.0 on the same length scale and combine the two Moho depth maps including a 1° buffer between them. We then interpolate between these smooth grids, across the buffer zone to avoid large Moho discontinuities where CRUST1.0 and the RF estimates disagree greatly.

Our bespoke Moho depth model (Figure S19) is then used to scale depths to layer interfaces within the ak135 velocity model above 120 km. We then follow methods previously used by Burdick et al. (2017) and Boyce et al. (2019) to impose our bespoke crustal model upon the adaptively parameterized grid within the final inversion.

Absolute arrival-time residuals are defined as $RES_{abs} = T_{abs} - T_{exp}$, where T_{abs} is the absolute arrival-time and T_{exp} is the expected arrival-time for a given reference Earth model. Vertically propagating P-waves are typically slower to travel through the upper 120 km of lithosphere within ak135 (Kennett et al., 1995) than through the same depth range within our receiver function derived bespoke Moho model (Figure S20). This results in a small positive travel-time correction to the residuals prior to inversion, because the value of T_{exp} is effectively lower. The shift towards increased delay-times due to mantle structure requires an apparent D.C. shift towards slower wavespeeds in the very shallow mantle of the crust corrected AFRP20 model. This effect is strongest beneath the oceans where Moho depths in CRUST1.0 (Laske et al., 2013) differ most strongly from ak135, a model more suited to the interpretation of continental data sets. Figure S21 demonstrates the effect of inclusion of the crustal correction on the output inversion in the shallow mantle.

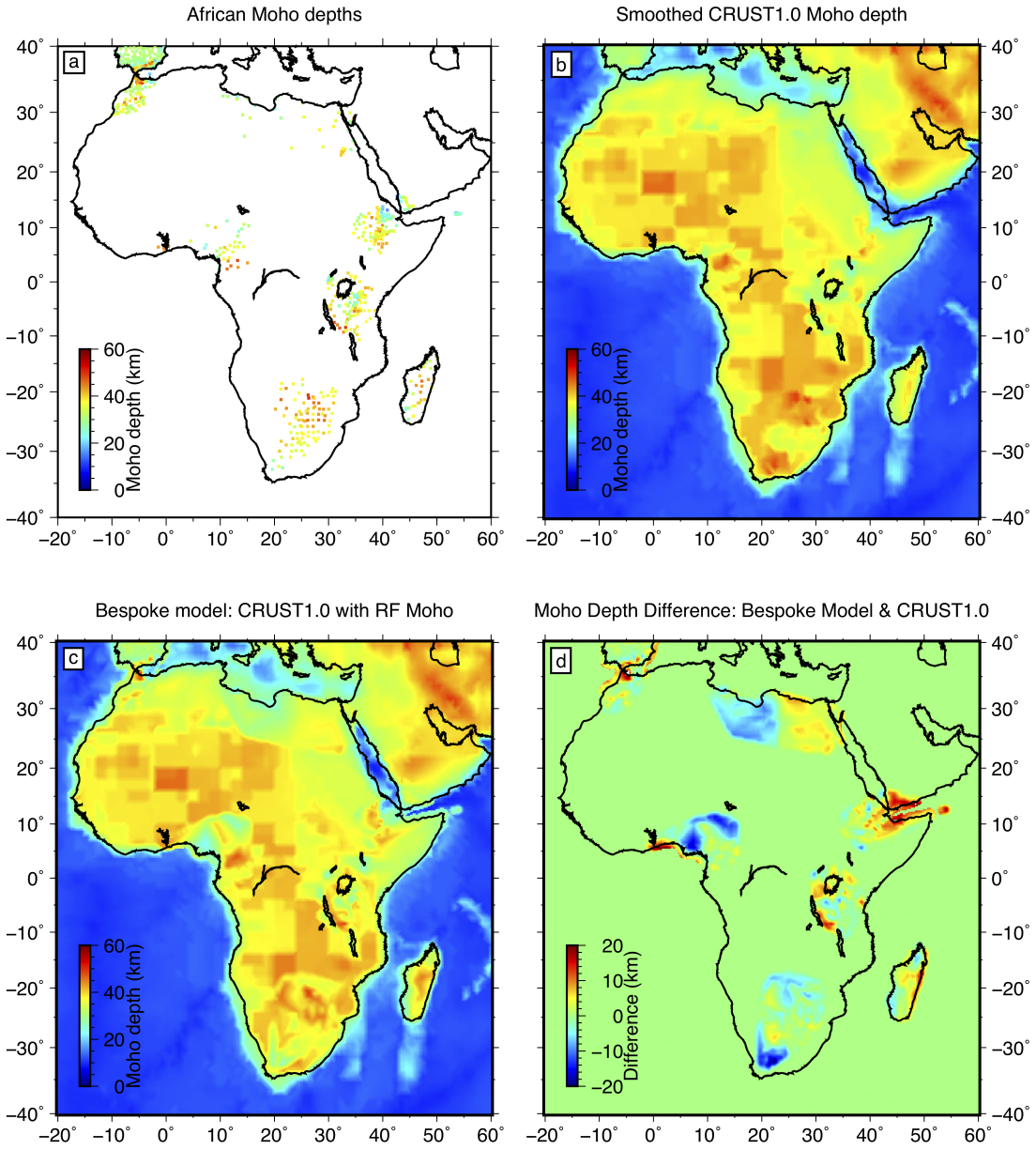

Figure S19. (*a*) Moho depth estimates from receiver functions compiled by Akpan et al. (2016); Hosny and Nyblade (2016); Andriampenomanana et al. (2017); Ebinger et al. (2017); Lemnifi et al. (2017); Fadel et al. (2018); Ogden et al. (2019). (*b*) CRUST1.0 (Laske et al., 2013) smoothed Moho depth map. (*c*) Bespoke crustal Moho map using receiver function estimates below seismic networks smoothed laterally into Crust1.0. (*d*) Difference between the bespoke Moho depth map and CRUST1.0. Positive values show CRUST1.0 to be anomalously thin compared to RF Moho depth estimates, whilst negative values show CRUST1.0 to be anomalously thick compared to RF Moho depths. Plots show individual data points within each table/grid to avoid displaying an overly smoothed output.

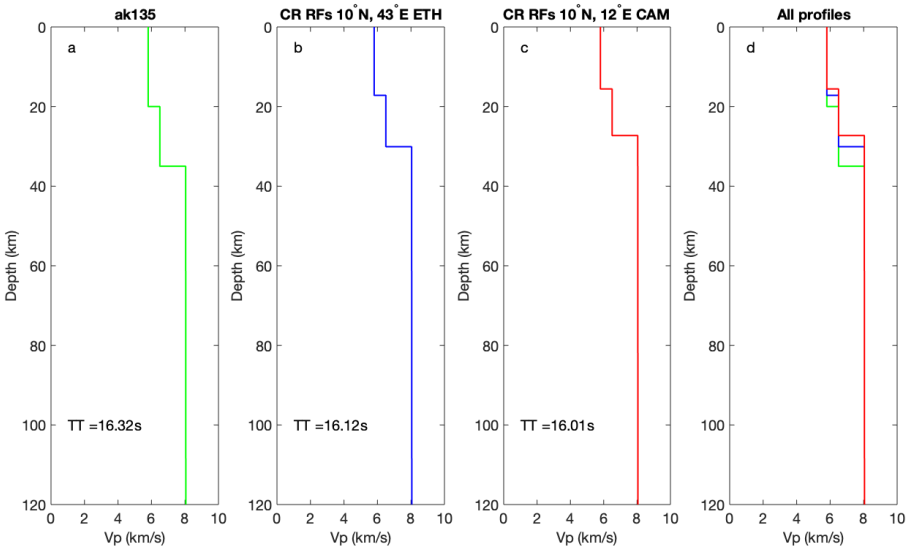

Figure S20. V_P velocity profiles as a function of depth for the upper 120 km of the ak135 1D model (*a*: Kennett et al., 1995) compared to specific locations within our receiver function derived bespoke Moho model above an upper mantle from ak135. The two central profiles are taken from approximate locations of Ethiopia (*b*: ETH: 10°N, 43°E) and the Cameroon Volcanic Line (*c*: CAM: 10°N, 12°E). Travel-times (in seconds) of a vertically propagating P-wave through the upper 120 km of each model are indicated. Three profiles are overlain in *d*.

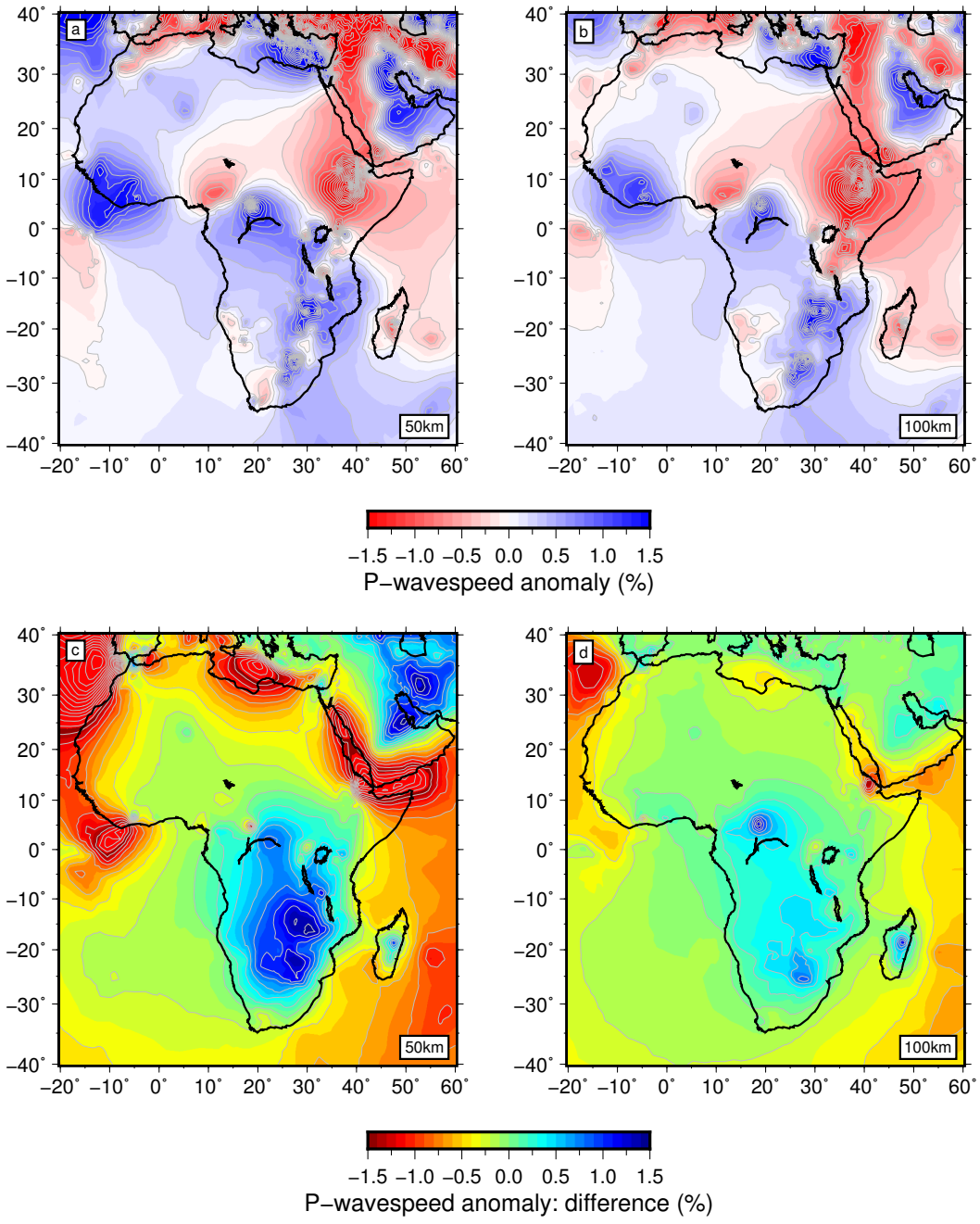

Figure S21. Figure to demonstrate the effect of the crustal correction on the tomographic inversion. The tomographic inversion without crustal correction for upper mantle depths (*a,b*) can be directly compared to AFRP20 including the crustal correction in Figure 5 of the main manuscript. The difference maps (*c,d*) are obtained by subtracting the inversion excluding crustal correction (e.g., *a,b*) from the inversion including crustal correction (Figure 5: main manuscript). Red/blue indicates the presented AFRP20 model (including crustal corrections) is slower/faster than the inversion that excludes crustal corrections (a,b).

9 Mantle Plume Resolution Tests

We further interrogate the sensitivity of AFRP20 to mantle plumes beneath the African plate (Figures S22–S25). We start with the same input model as outlined in the main Manuscript (including two elliptical, inclined slow wavespeed anomalies extending from the surface to the core-mantle boundary and approximate major upper mantle anomalies seen in AFPR20) and make modifications where mentioned. We also render the δV_P = –2.0% wavespeed anomaly contour within the two plume synthetic structure in 3-D for enhanced visualization of the input model (Figure S26).

The upper mantle CVL anomaly is smeared vertically to transition zone depths (<660 km: Figure S22). Amplitude recovery for the CVL is <50%. At mid mantle depths (∼1000 km) lateral smearing does occur but slow mid-mantle wavespeeds associated with the synthetic African Superplume structure to the east are not smeared laterally to directly below the CVL.

When progressively increasing gap thickness between upper- and lower-mantle slow wavespeeds, anomalies can be distinguished visually when separated by gap widths of ≥300 km (Figure S23). Progressively moving a 300 km horizontal gap from the upper to lower mantle shows that a 300 km thick or narrower gap is identified by a significant amplitude reduction because significant vertical smearing exists across the gap, particularly for the wider planform southerly anomaly at gap widths of 300–500 km (Figure S24). Across all tests, recovery amplitudes of the slow wavespeed anomalies are typically >90% above but often less below the gap.

To explore the sensitivity of AFRP20 to the presence of a ponded slow wavespeed anomaly below centered at lower mantle transition zone depths we again modify our "two plume" synthetic wavespeed anomaly structure with a pervasive slow wavespeed anomaly in East Africa (Figure S25a,b,c). Slow wavespeeds are vertically smeared, but the affect appears stronger in the upwards direction from lower mantle transition zone depths (Figure S25). Focusing on wavespeeds below the Turkana Depression (around 5°N, 35°E), recovered peak low wavespeed anomalies at 700 km depth are δV_P ≈–1.5%, decaying to ≈–0.5% at 750 km depth (Figure S25d,e), i.e. while the input "ponded" slow wavespeed anomaly is partially smeared downwards, amplitudes are <25%. Comparing this resolution test to AFRP20 (Figure S25g,h,i), little variation in slow wavespeed anomalies is seen at 700 km between the Turkana Depression and below the Ethiopian and Kenyan Plateaus –2%≤ δV_P ≤–1.5%. At 750 km depth slow wavespeed anomaly amplitudes are δV_P ≈–0.5% directly below Turkana separating two regions of significantly slower anomalies below Ethiopia and Kenya (–1.6%≤ δV_P ≤–1.2%). Due to our vertical parameterization (45 km) there is little observable difference between AFRP20 at 660 km (Figure 6b) and at 700 km (Figure S25g). However this resolution test indicates that a ponded layer with thickness greater than our depth parameterization (∼50 km) at or below the base of the mantle transition zone is not clearly apparent in AFRP20.

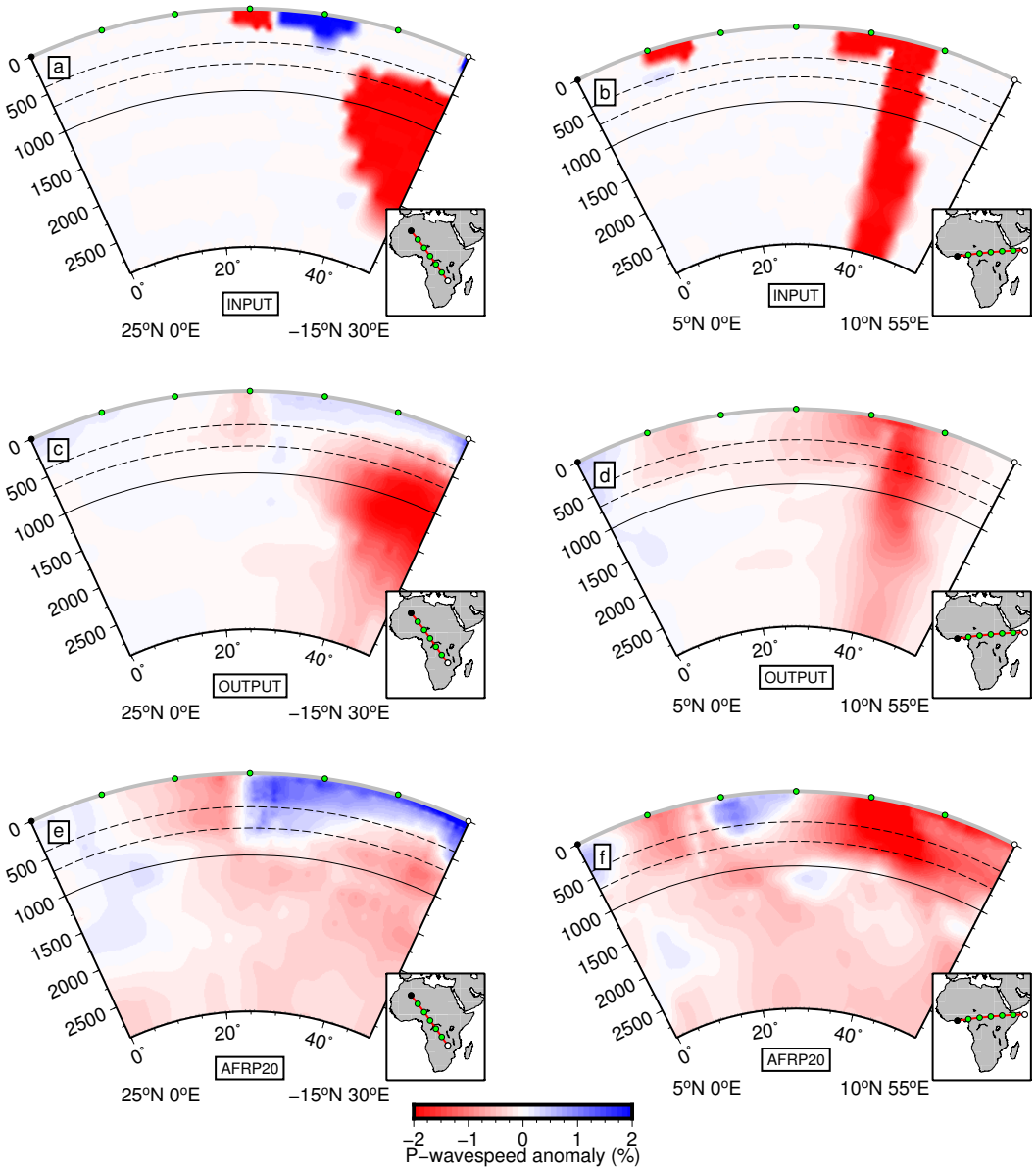

Figure S22. Figure to show perpendicular (*a,c,e*) and parallel (*b,d,f*) P-wave wavespeed structure beneath the Cameroon Volcanic Line within the input (*a,b*) and output (*c,d*) "two plume" resolution test and AFRP20 tomographic model (*e,f*) shown in the main manuscript. Visual defects within the input anomaly model result from a coarse adaptive grid in poorly sampled regions - Figure S17. The cross section locations are indicated in the lower portion of each sub-figure. Please note the African Superplume input structure is not cut at right-angles in cross section (*a*) but is identical to that shown in Figure S26 and in the main manuscript.

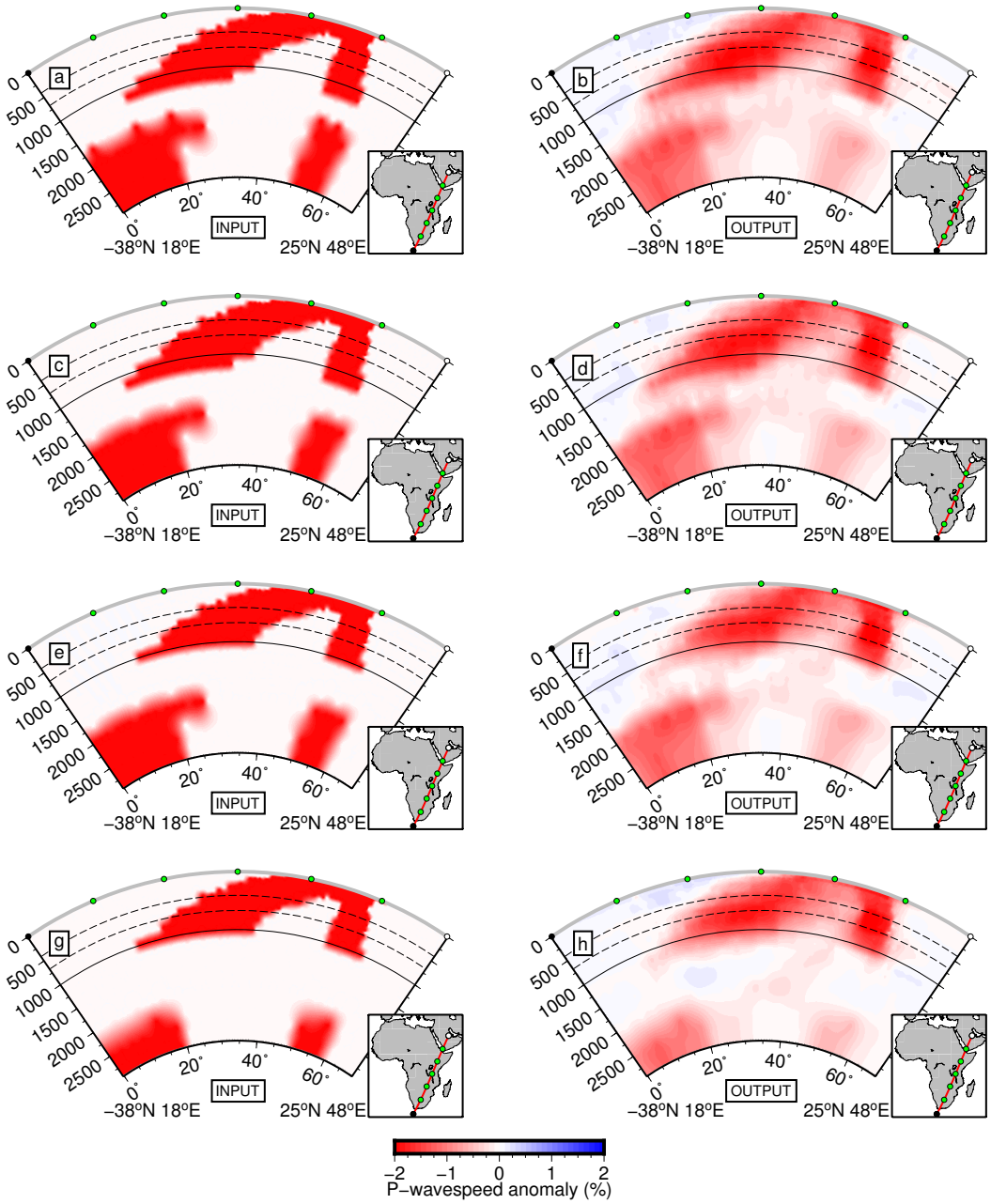

Figure S23. An inclined, elliptical, input slow wavespeed anomaly ($\delta V_P = -2.0\%$) increases in areal extent from the surface, centered at 10°N, 40°E to the core-mantle boundary centered at –35°N, 15°E. Also added is a narrower planform, more steeply dipping slow wavespeed anomaly ($\delta V_P = -2.0\%$) extending from the surface, centered at 10°N, 42°E to the core-mantle boundary centered at 13°N, 44°E. We modify this structure by removing any slow wavespeed anomalies (imposing a $\delta V_P = 0.0\%$ constraint) in the mid-mantle centered at 1500 km depth using increasing thicknesses from top-to-bottom in the figure (Thicknesses: 300 km, 500 km, 700 km, 1000 km). Visual defects within the input anomaly model result from a coarse adaptive grid in poorly sampled regions - Figure S17. The cross section location is indicated beside each sub-figure. Input anomalies (*a,c,e,g*) are displayed on the same color scale as the recovered anomalies (*b,d,f,h*).

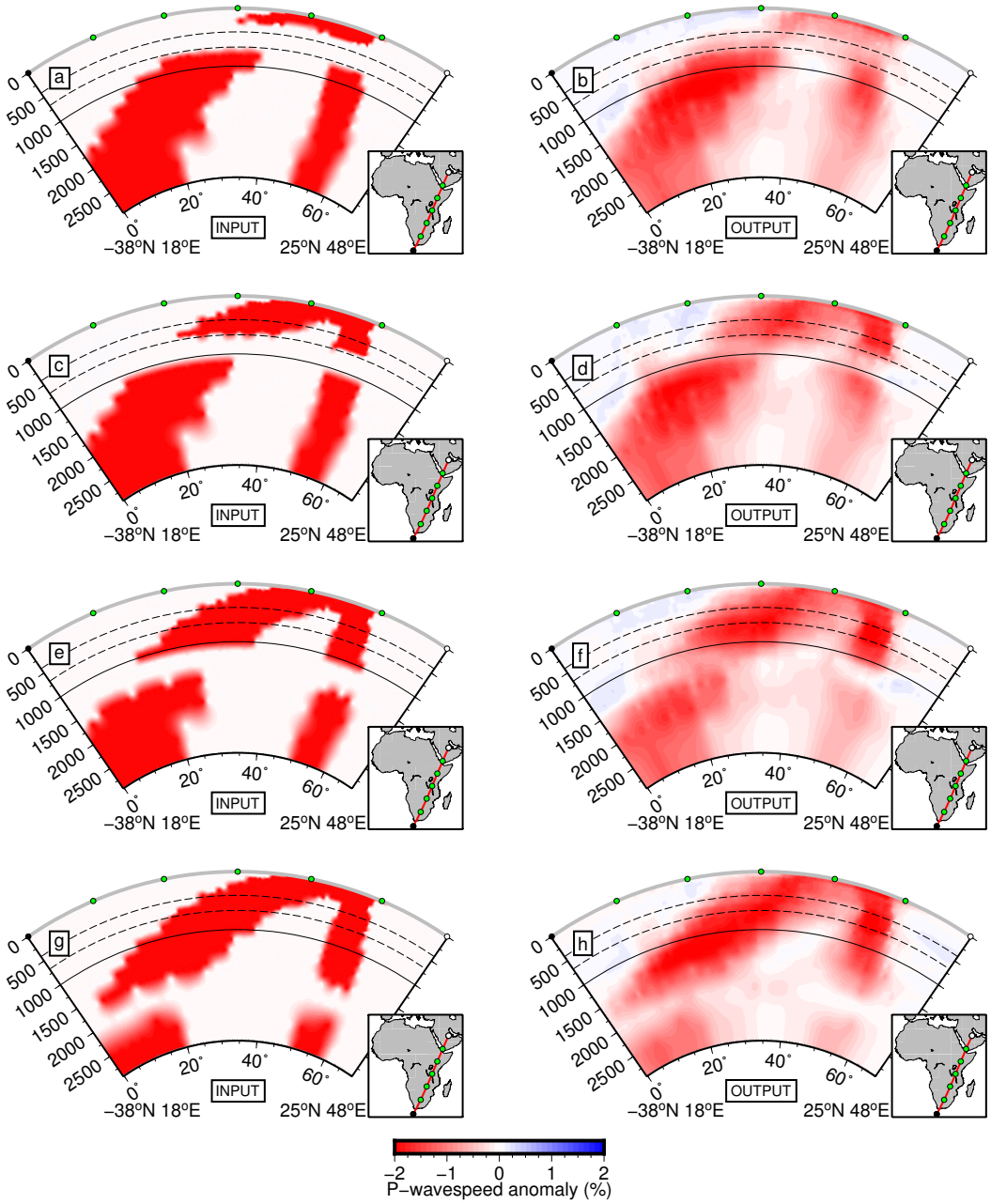

Figure S24. An inclined, elliptical, input slow wavespeed anomaly (δV_P = –2.0%) increases in areal extent from the surface, centered at 10°N, 40°E to the core-mantle boundary centered at –35°N, 15°E. Also added is a narrower planform, more steeply dipping slow wavespeed anomaly (δV_P = –2.0%) extending from the surface, centered at 10°N, 42°E to the core-mantle boundary centered at 13°N, 44°E. We modify this structure by removing any slow wavespeed anomalies (imposing a δV_P = 0.0% constraint) in the mid-mantle centered at 500 km, 900 km, 1300 km, 1900 km depths (figure top-to-bottom) using a 300 km thickness. Visual defects within the input anomaly model result from a coarse adaptive grid in poorly sampled regions - Figure S17. The cross section location is indicated beside each sub-figure. Input anomalies (*a,c,e,g*) are displayed on the same color scale as the recovered anomalies (*b,d,f,h*).

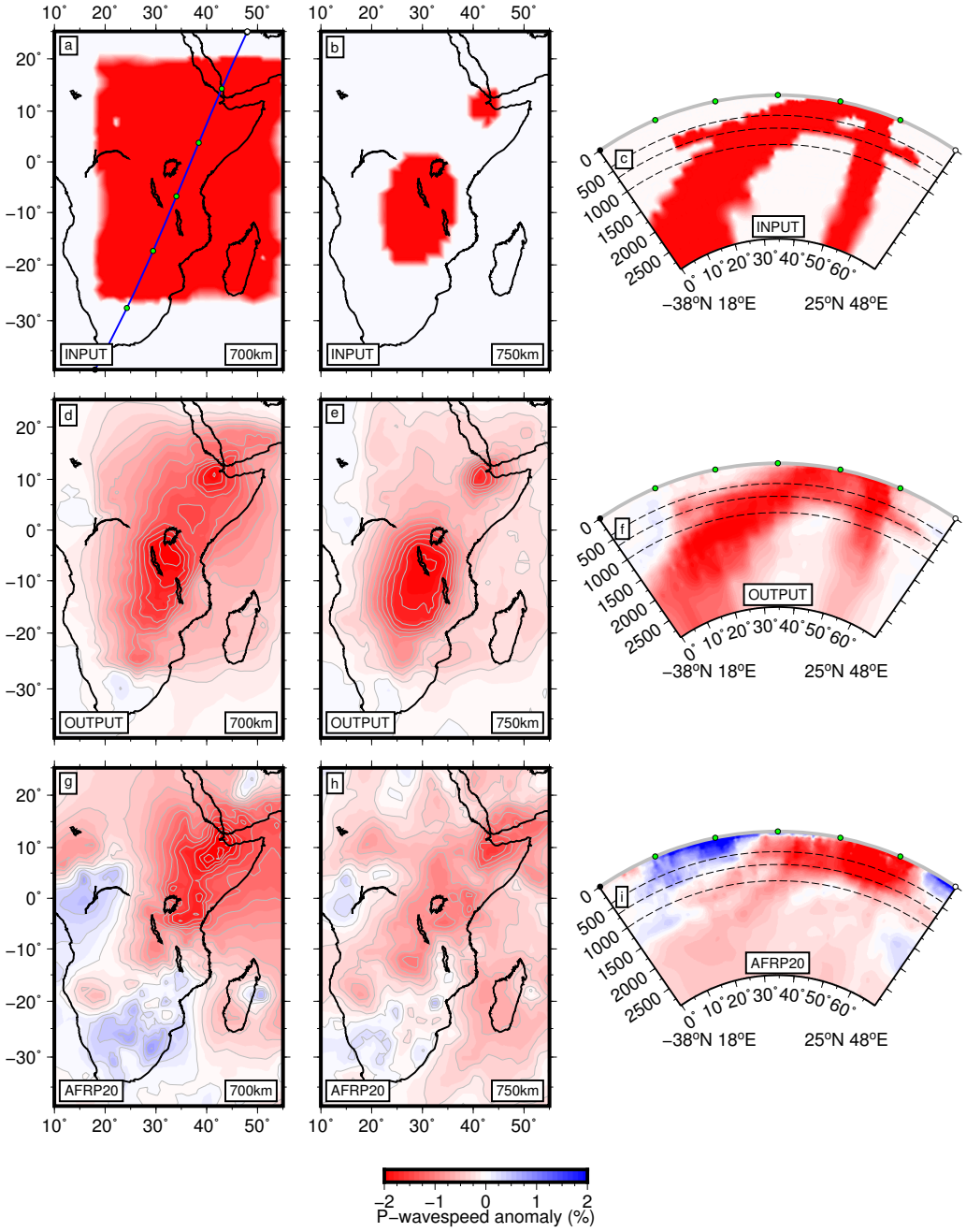

Figure S25. An inclined, elliptical, input slow wavespeed anomaly ($\delta V_P = -2.0\%$) increases in areal extent from the surface, centered at 10°N, 40°E to the core-mantle boundary centered at –35°N, 15°E. Also added is a narrower planform, more steeply dipping slow wavespeed anomaly ($\delta V_P = -2.0\%$) extending from the surface, centered at 10°N, 42°E to the core-mantle boundary centered at 13°N, 44°E. We modify this structure by adding a pervasive slow wavespeed anomaly through East Africa centered at lower mantle transition zone depths (500-700 km depth). Visual defects within the input anomaly model result from a coarse adaptive grid in poorly sampled regions - Figure S17. The cross section location is indicated in (*a*). Input anomalies (*a,b,c*) are displayed on the same color scale as the recovered anomalies (*d,e,f*) and AFRP20 (*g,h,i*).

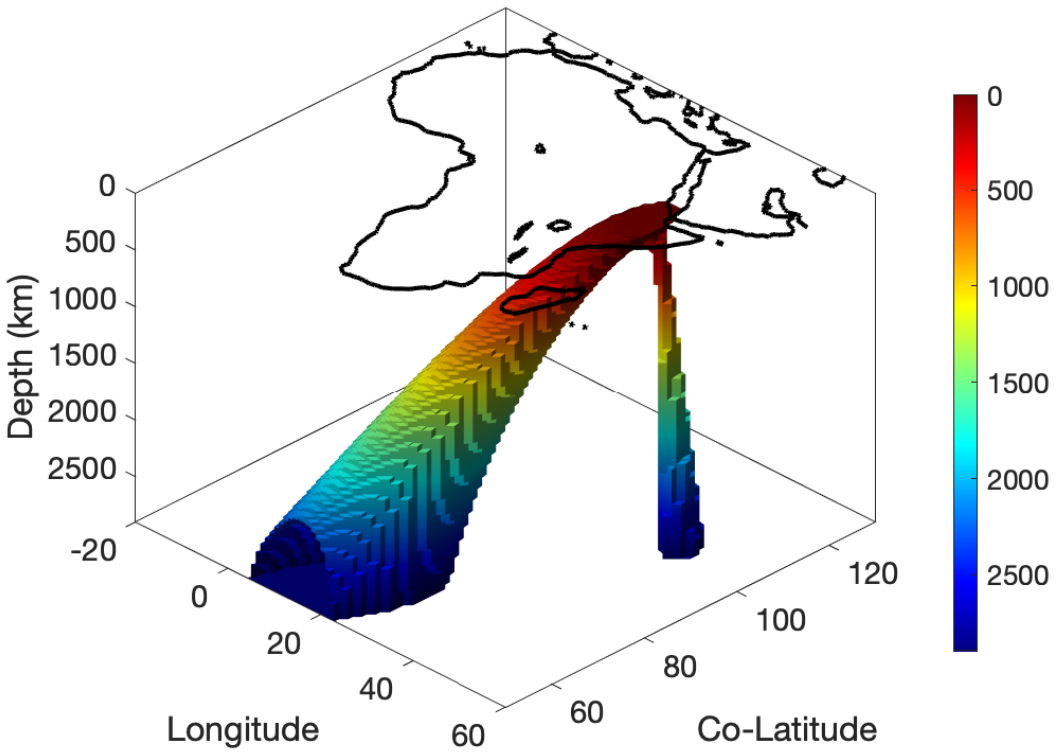

Figure S26. 3-D render of the $\delta V_P = -2.0\%$ wavespeed anomaly contour within the two whole-mantle plume synthetic structure beneath Africa. Colors within the model volume represent depth within the mantle.

10 Checkerboard Resolution Tests

Checkerboard input models are constructed by distributing alternating $\delta V_P = \pm 2\%$ wavespeed anomalies of 200 km thickness throughout the model space at 200 km, 600 km and 900 km depth. Lateral anomaly length scales vary from 2–10° (Figures S27–S31). Anomalies of size 2° width are spatially well recovered at 200 km depth with amplitudes of ∼50% in densely instrumented regions: Ethiopia, eastern and southern Africa and parts of Madagascar (Figure S27). Amplitudes of 3° anomalies are well recovered (∼50–75% amplitude) at 200 km depth below densely instrumented regions, including the Atlas mountains (Figure S28). Amplitude recovery is ∼50% at 600 km depth but anomalies are well recovered spatially. Anomalies of 5° width show reasonable spatial recovery at 200 km depth but lose amplitude (to <<50%) outside densely instrumented regions. At 600 km and 900 km depth, amplitude recovery is ≥50% with reasonable spatial recovery. 5° anomalies are resolvable in depth (Figure S29) although some vertical smearing occurs. 7.5° and 10° anomalies show good recovery of sharp anomaly boundaries at 200 km and 600 km depth beneath the densest networks (Figure S30–S31). At 900 km depth, amplitude recovery is ∼50% everywhere below Africa with good spatial recovery, except beneath the western-most part where station density is low. In the upper mantle, 7.5° and 10° anomalies are resolvable in depth, but mid-mantle anomalies exhibit some vertical smearing of ∼100–200 km.

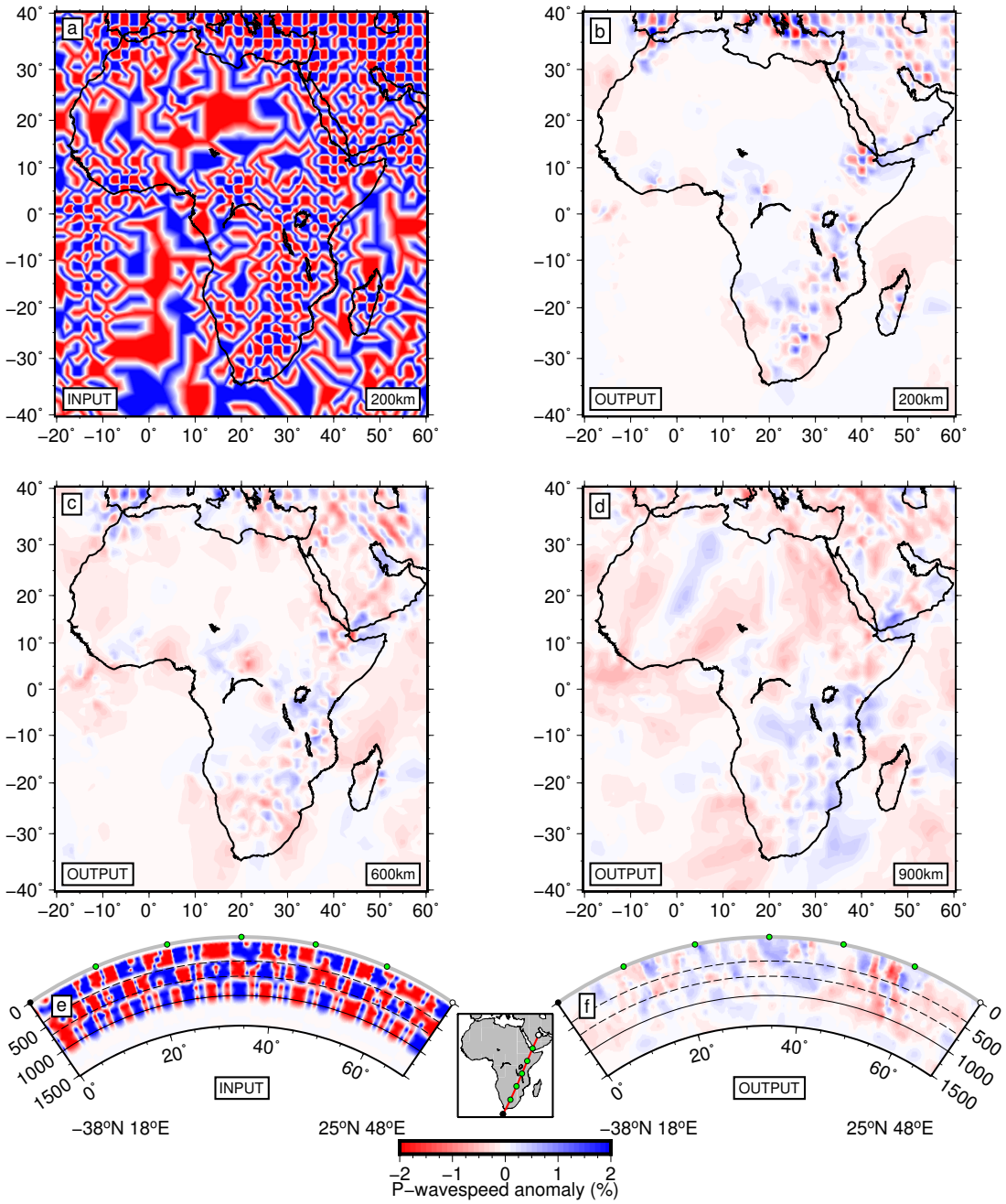

Figure S27. African checkerboard resolution tests using $\delta V_P = \pm 2.0\%$ input wavespeed anomalies of 2° width. Positive and negative input anomalies are arranged in an alternating grid at 200 km, 600 km and 900 km depth and are displayed in map (*a*) and cross section along the SW-NE profile (*e*). Visual defects within the input anomaly model result from a coarse adaptive grid in poorly sampled regions - Figure S17. Recovered anomalies (*b–d,f*) are displayed on the same color scale as the input.

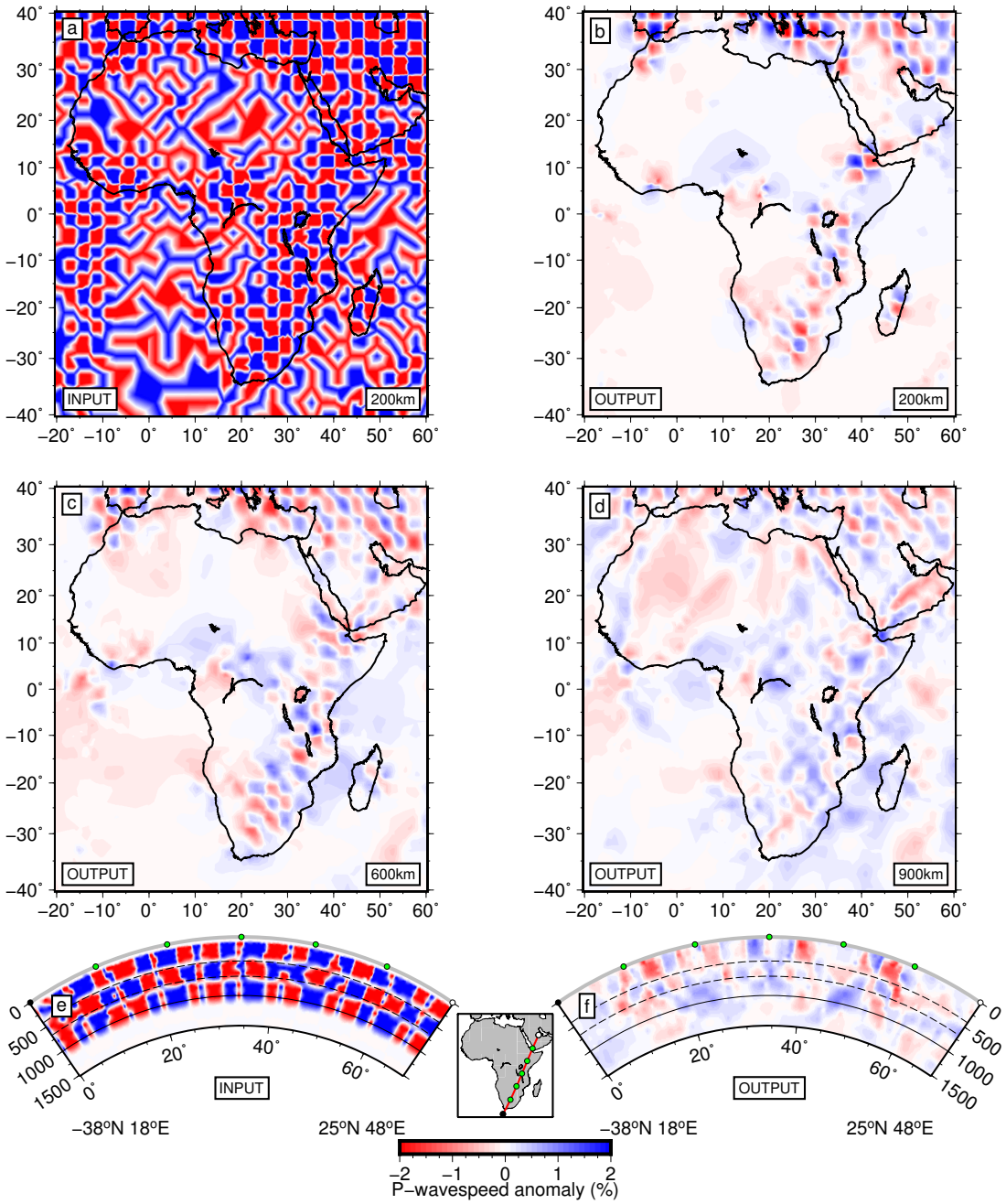

Figure S28. African checkerboard resolution tests using $\delta V_P = \pm 2.0\%$ input wavespeed anomalies of 3° width. Positive and negative input anomalies are arranged in an alternating grid at 200 km, 600 km and 900 km depth and are displayed in map (*a*) and cross section along the SW-NE profile (*e*). Visual defects within the input anomaly model result from a coarse adaptive grid in poorly sampled regions - Figure S17. Recovered anomalies (*b–d,f*) are displayed on the same color scale as the input.

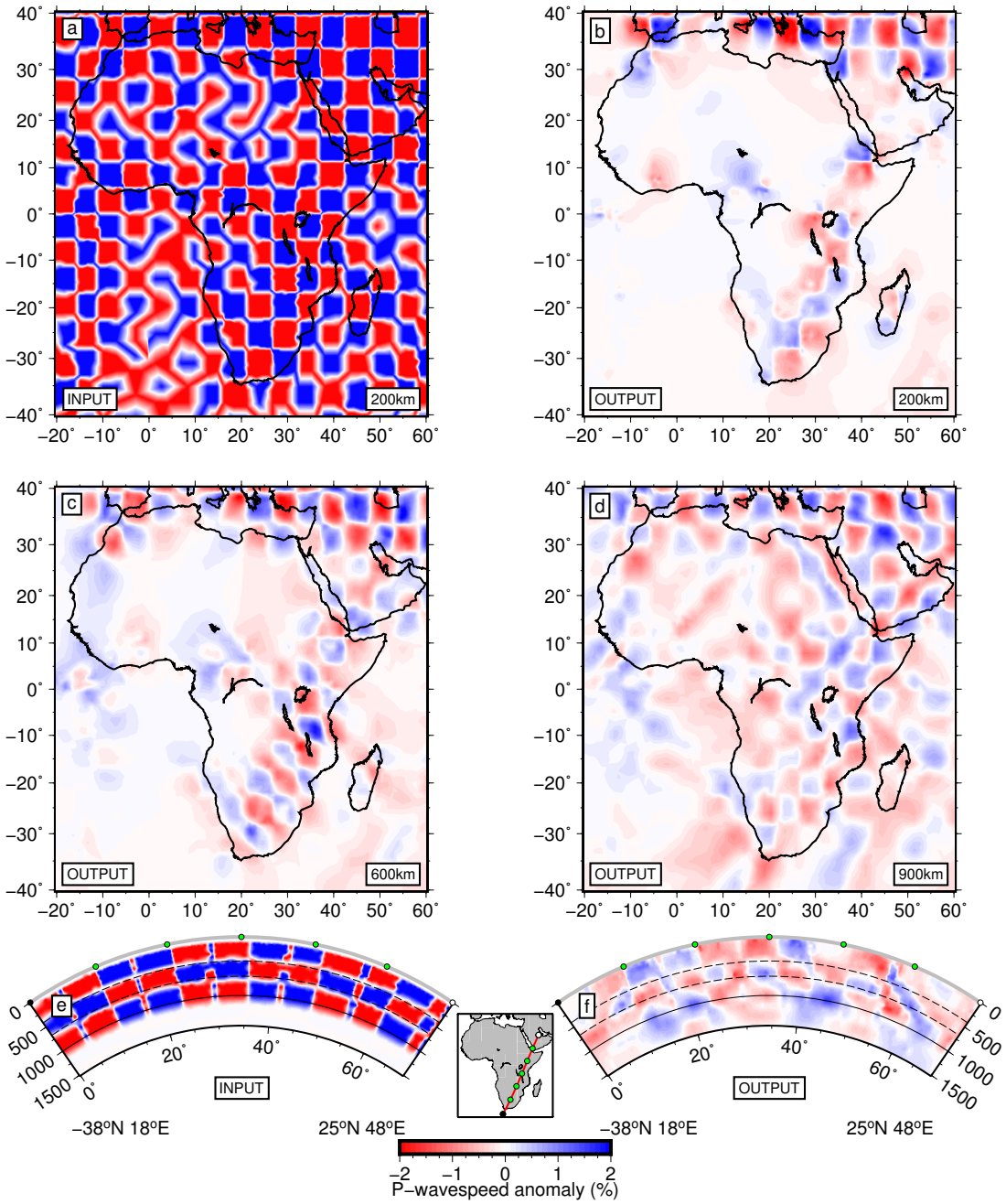

Figure S29. African checkerboard resolution tests using $\delta V_P = \pm 2.0\%$ input wavespeed anomalies of 5° width. Positive and negative input anomalies are arranged in an alternating grid at 200 km, 600 km and 900 km depth and are displayed in map (*a*) and cross section along the SW-NE profile (*e*). Visual defects within the input anomaly model result from a coarse adaptive grid in poorly sampled regions - Figure S17. Recovered anomalies (*b–d,f*) are displayed on the same color scale as the input.

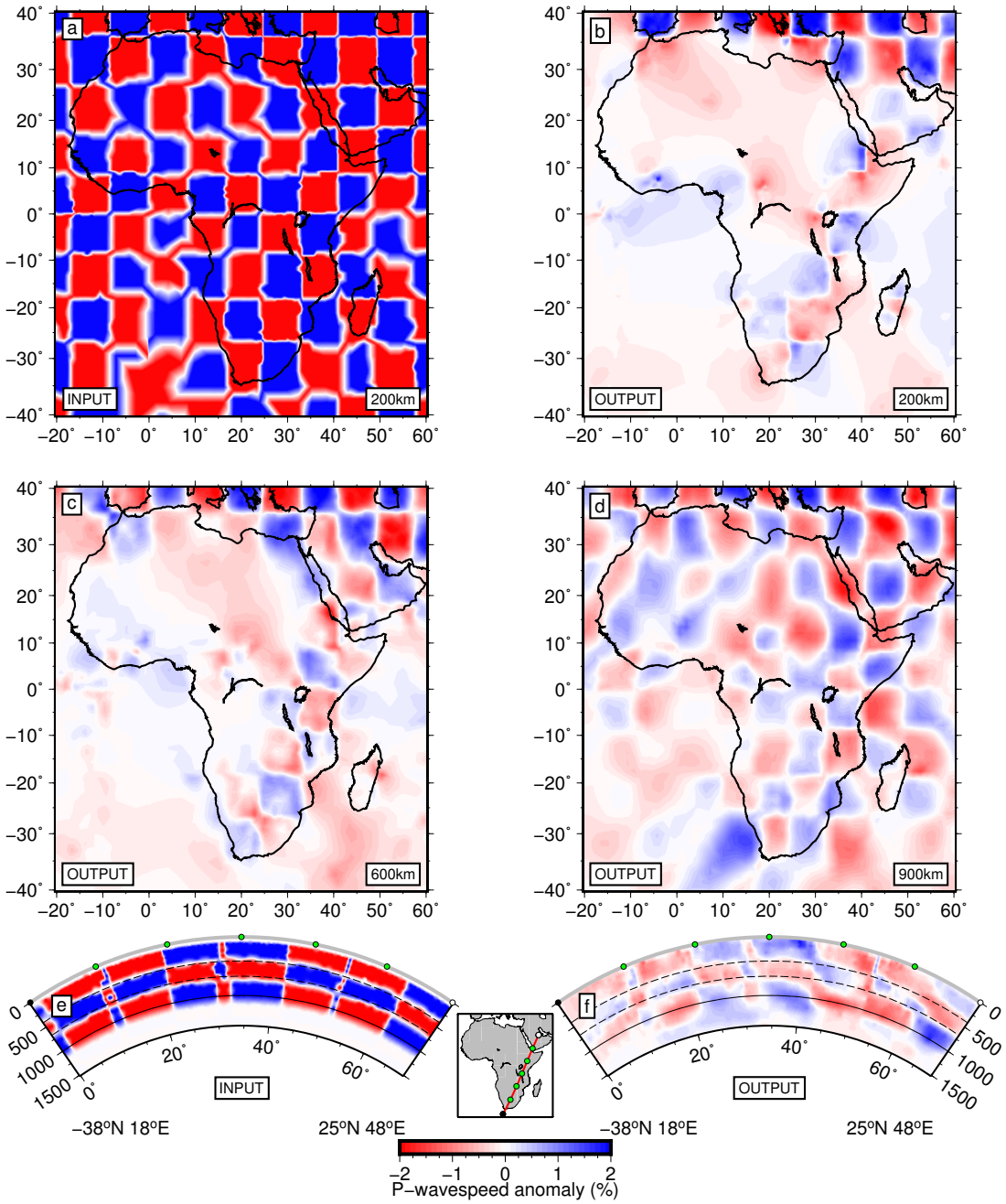

Figure S30. African checkerboard resolution tests using $\delta V_P = \pm 2.0\%$ input wavespeed anomalies of 7.5° width. Positive and negative input anomalies are arranged in an alternating grid at 200 km, 600 km and 900 km depth and are displayed in map (*a*) and cross section along the SW-NE profile (*e*). Visual defects within the input anomaly model result from a coarse adaptive grid in poorly sampled regions - Figure S17. Recovered anomalies (*b–d,f*) are displayed on the same color scale as the input.

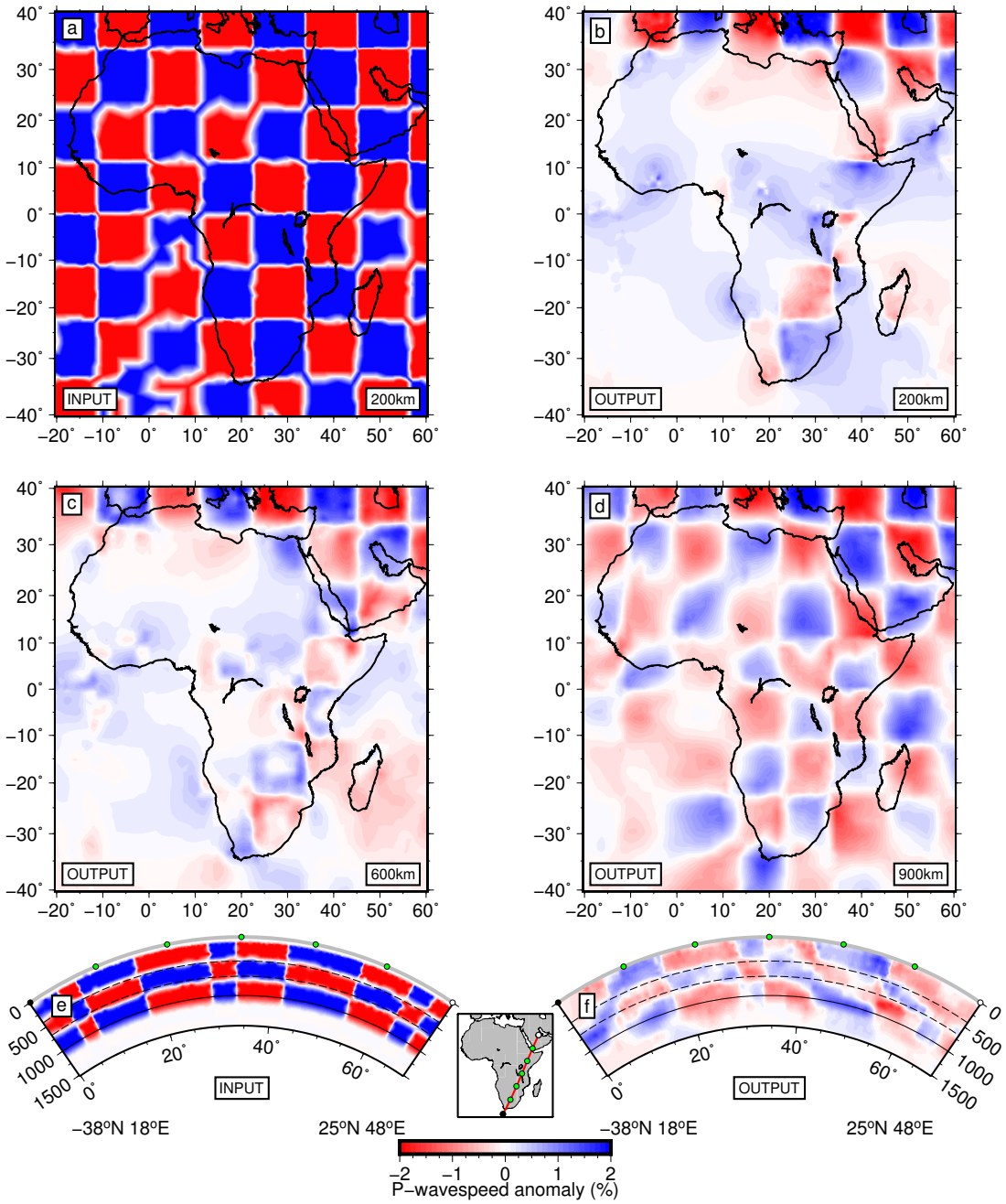

Figure S31. African checkerboard resolution tests using $\delta V_P = \pm 2.0\%$ input wavespeed anomalies of 10° width. Positive and negative input anomalies are arranged in an alternating grid at 200 km, 600 km and 900 km depth and are displayed in map (*a*) and cross section along the SW-NE profile (*e*). Visual defects within the input anomaly model result from a coarse adaptive grid in poorly sampled regions - Figure S17. Recovered anomalies (*b–d,f*) are displayed on the same color scale as the input.

11 Upper Mantle Resolution Tests

To further explore the sensitivity of AFRP20 to wavespeed structure below the Tanzanian craton we construct synthetic models with $\delta V_P = +2\%$ wavespeed anomalies using oval and rectangular planforms with increasing thicknesses (Figures S32–S34). We also introduce an underlying $\delta V_P = -2\%$ wavespeed anomaly beneath the craton to simulate hot mantle plume material beneath the African plate (Figure S34). Using either a larger oval or smaller rectangular input anomaly planform, amplitude recovery is ∼50% beneath the dense seismograph networks (Figures S32–S33) at all but the shallowest depths. Lateral smearing does occur beyond the seismograph network footprint. Inherent vertical smearing is approximately double the anomaly input thickness. When underlain by a slow wavespeed anomaly (Figure S34) the depth extent of the fast wavespeed anomaly is well resolved to within ≤100 km of the input model. Vertical smearing of the underlying slow wavespeed anomaly is strong. An underlying slow wavespeed anomaly reduces lateral smearing of the overlying fast wavespeed anomaly but amplitude recovery is reduced to ∼30%.

For the Madagascan case (Figure S35), we construct synthetic models with a rectangular slow wavespeed anomaly of $\delta V_P = -2.0\%$ centered at –20°N, 47°E and rectangular fast wavespeed anomaly of $\delta V_P = +2.0\%$ centered at –17.5°N, 49°E. We vary the depth extent of anomalies to test vertical smearing. Peak amplitude recovery for the slow wavespeed anomaly is <50% but is well constrained laterally while the fast wavespeed anomaly is less well constrained laterally but displays >50% peak amplitude recovery. Vertical smearing of the shallow wavespeed anomalies is up to twice the input anomaly thickness (Figure S35d). The deeper wavespeed anomalies show upward smearing towards the surface from 100 km depth but are better resolved with depth at their base (∼ ±100 km) with very low amplitude leakage along particularly prominent ray paths (Figure S35f). Based on these tests we cannot conclusively conclude that the fast wavespeed anomaly below Madagascar (Figure S35g,h) is an artifact of our model. Furthermore, if slow wavespeed anomalies were limited to the upper mantle below central Madagascar (<660 km depth) we expect a significant reduction in anomaly amplitude in AFRP20. AFRP20 is not able to determine whether the shallow slow wavespeed anomaly beneath central Madagascan volcanism connects to the surface due to upward smearing present.

Figures S36–S37 explore the sensitivity of AFRP20 to separation of slow wavespeed anomalies in the upper mantle below the Turkana Depression where seismic station coverage is lacking. For the case of two slow wavespeed anomalies below the Ethiopian and Kenyan plateaus (Figure S36), recovered anomaly amplitudes are $\delta V_P \approx$–1.5% (∼75%). Below station coverage these anomalies are well constrained laterally. Vertical smearing is ∼100–200 km below the upper mantle. Below the Turkana Depression (where stations are presently lacking) some smearing of adjacent wavespeed anomalies does occur laterally, peaking around δV_P<–0.75% at shallow depths (∼100 km) but decaying to δV_P<–0.2% at transition zone depths. Amplitude leakage between the Ethiopian and Kenyan plateaus is 35–10% of the adjacent input anomalies in this test. If this case were to be sampled by the real data, AFRP20 would show a significant amplitude reduction below the Turkana Depression in the upper mantle.

Although the single slow wavespeed anomaly below the Turkana Depression is not well constrained laterally to the east and west (Figure S37) peak amplitude recovery is $\delta V_P \approx$–1.25% (>60%). Lateral smearing to the north and south at upper mantle depths is very limited due to the stations overlying adjacent regions. However some slow wavespeed material is smeared laterally at 600–900 km depth towards the northeast. These tests (Figures S36–S37) suggest that AFRP20 is sensitive to upper mantle wavespeed structure below the Turkana Depression despite the lack of overlying stations.

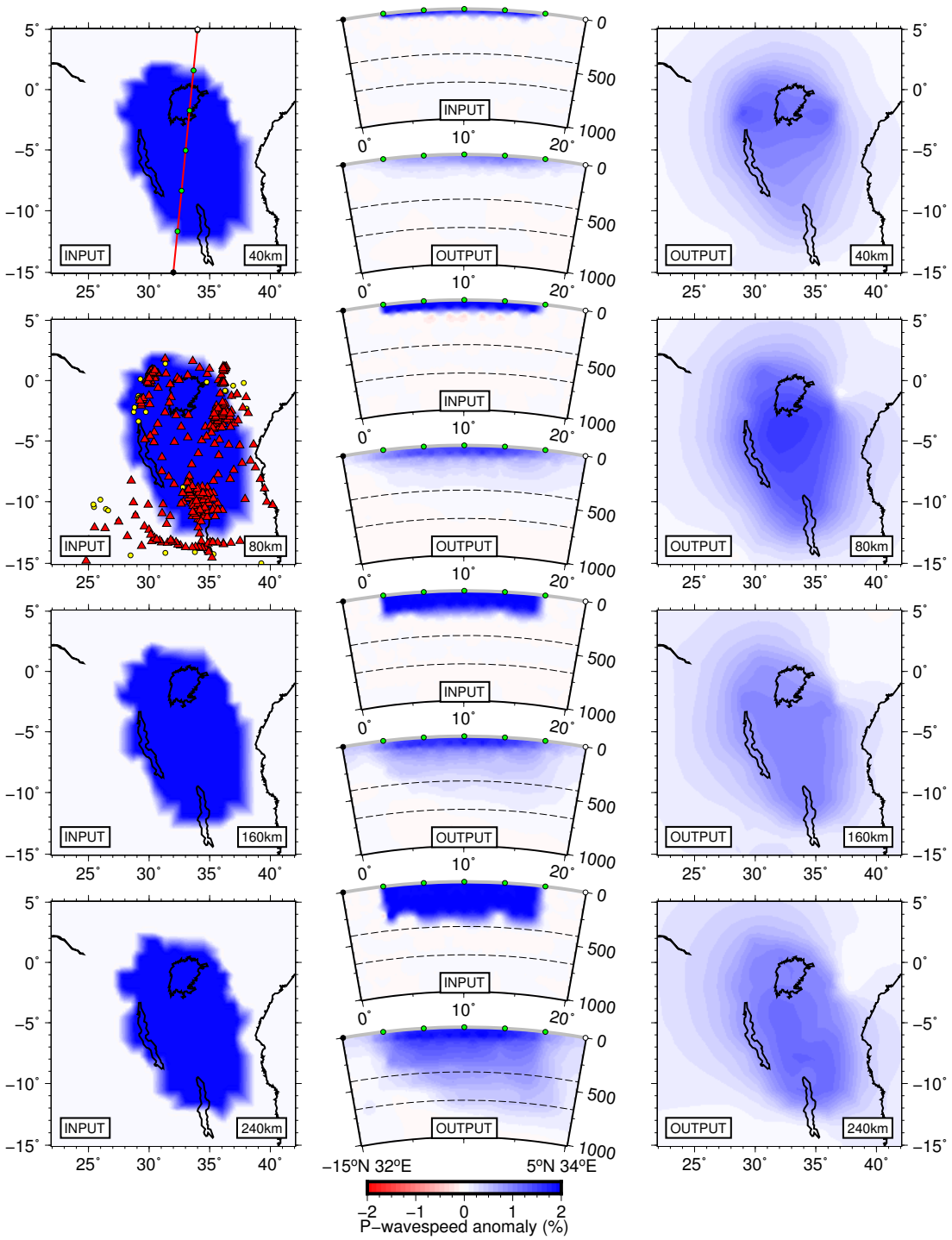

Figure S32. Resolution test for the Tanzanian craton using an input wavespeed anomaly of $\delta V_P = +2.0\%$ and elliptical planform. Input craton anomaly thicknesses are 50 km, 100 km, 200 km, 300 km shown on the *LHS* and upper cross section of each model row. Recovered anomalies shown on the lower cross section of each row and *RHS* are displayed with the same color scale as the input. The location of cross sections used is marked by the red line on the 40 km depth input anomaly map. Yellow circles and red triangles on the 80 km depth input anomaly map show the locations of "EHB" stations and temporary deployments analyzed in this study (Figures S8, S14).

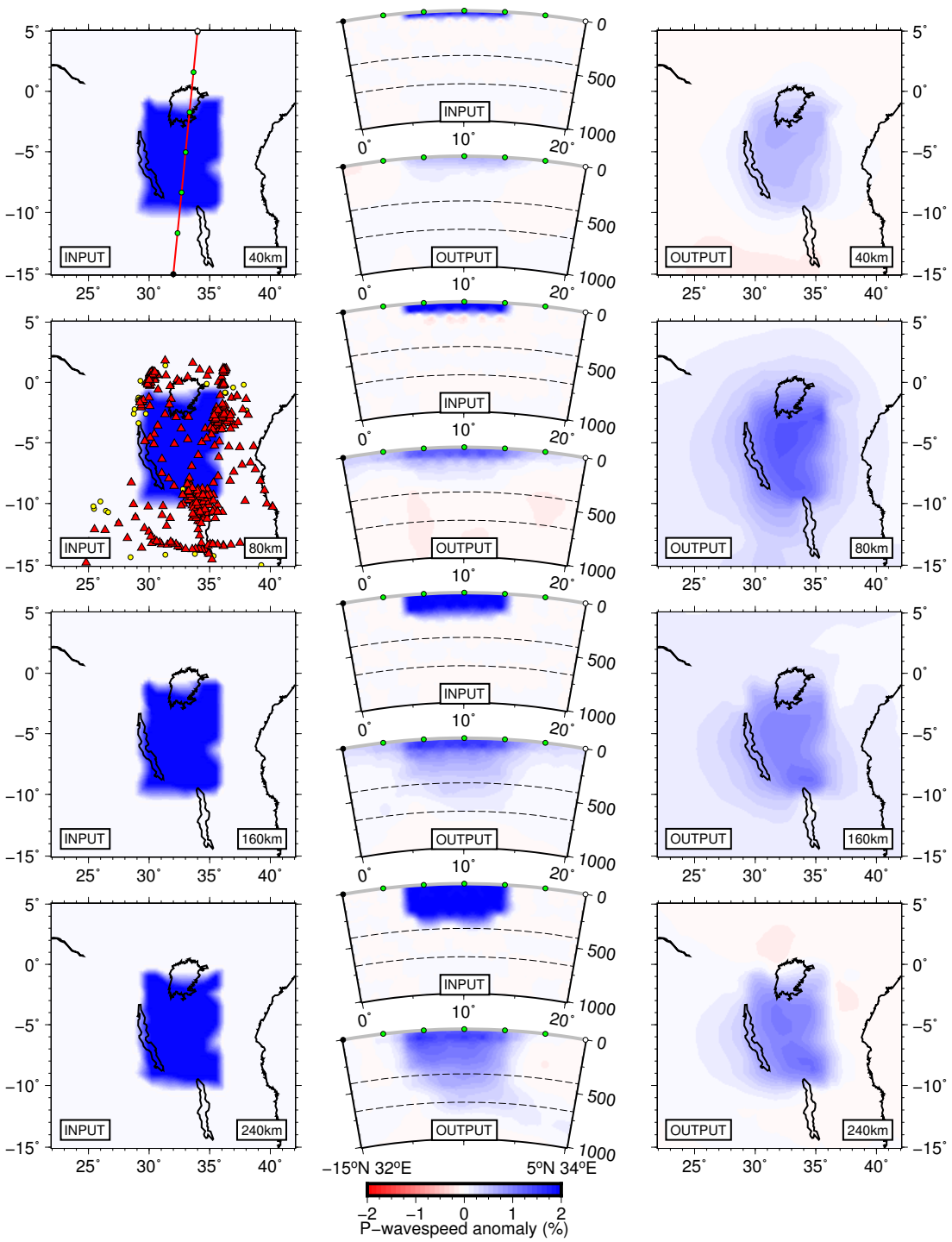

Figure S33. Resolution test for the Tanzanian craton using an input wavespeed anomaly of $\delta V_P = +2.0\%$ and rectangular planform. Input craton anomaly thicknesses are 50 km, 100 km, 200 km, 300 km shown on the *LHS* and upper cross section of each model row. Recovered anomalies shown on the lower cross section of each row and *RHS* are displayed with the same color scale as the input. The location of cross sections used is marked by the red line on the 40 km depth input anomaly map. Yellow circles and red triangles on the 80 km depth input anomaly map show the locations of "EHB" stations and temporary deployments analyzed in this study (Figures S8, S14).

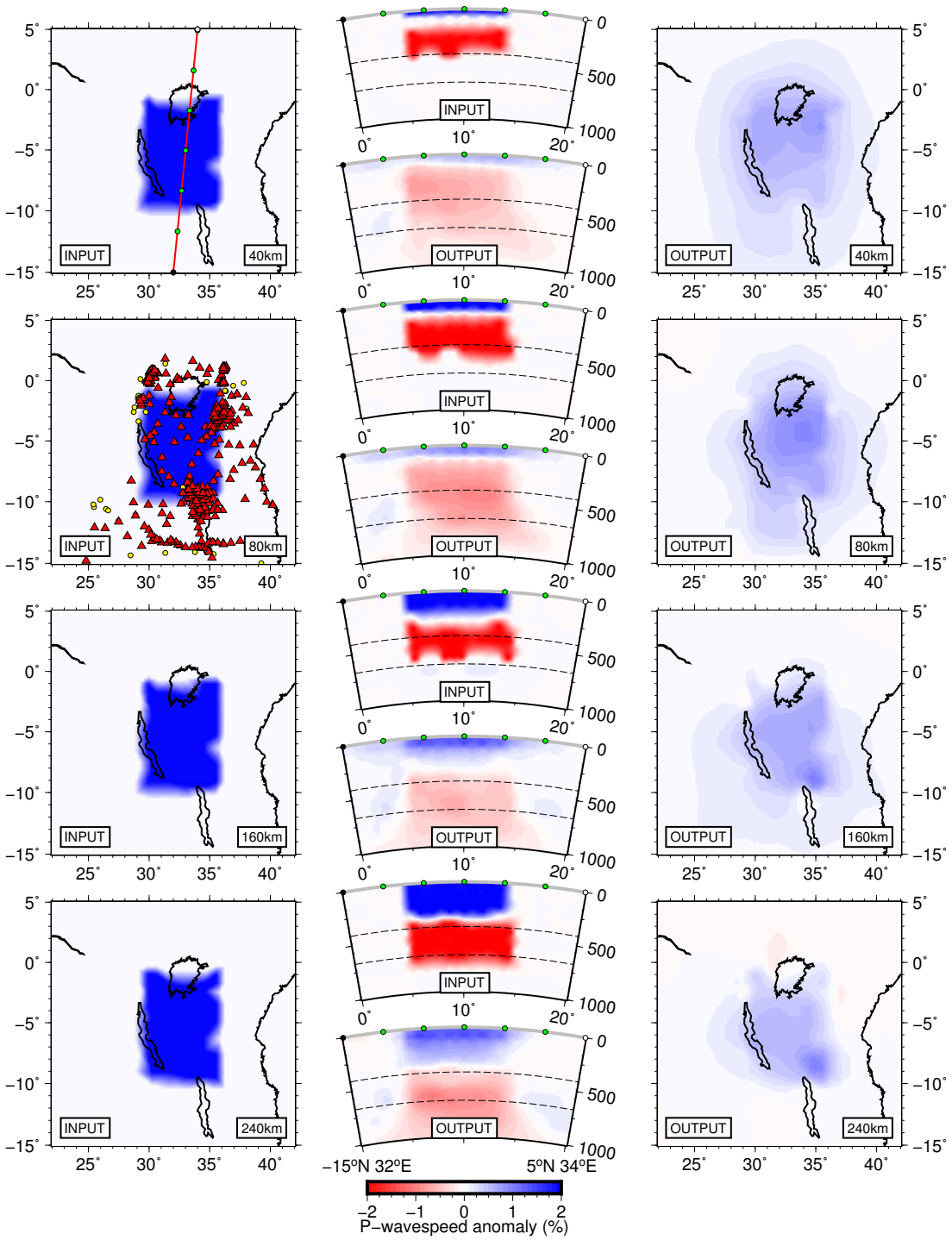

Figure S34. Resolution test for the Tanzanian craton using an input wavespeed anomaly of $\delta V_P = +2.0\%$ and rectangular planform. Directly beneath we include a 300 km thick $\delta V_P = -2.0\%$ wavespeed anomaly. Input craton anomaly thicknesses are 50 km, 100 km, 200 km, 300 km shown on the *LHS* and upper cross section of each model row. Recovered anomalies shown on the lower cross section of each row and *RHS* are displayed with the same color scale as the input. The location of cross sections used is marked by the red line on the 40 km depth input anomaly map. Yellow circles and red triangles on the 80 km depth input anomaly map show the locations of "EHB" stations and temporary deployments analyzed in this study (Figures S8, S14).

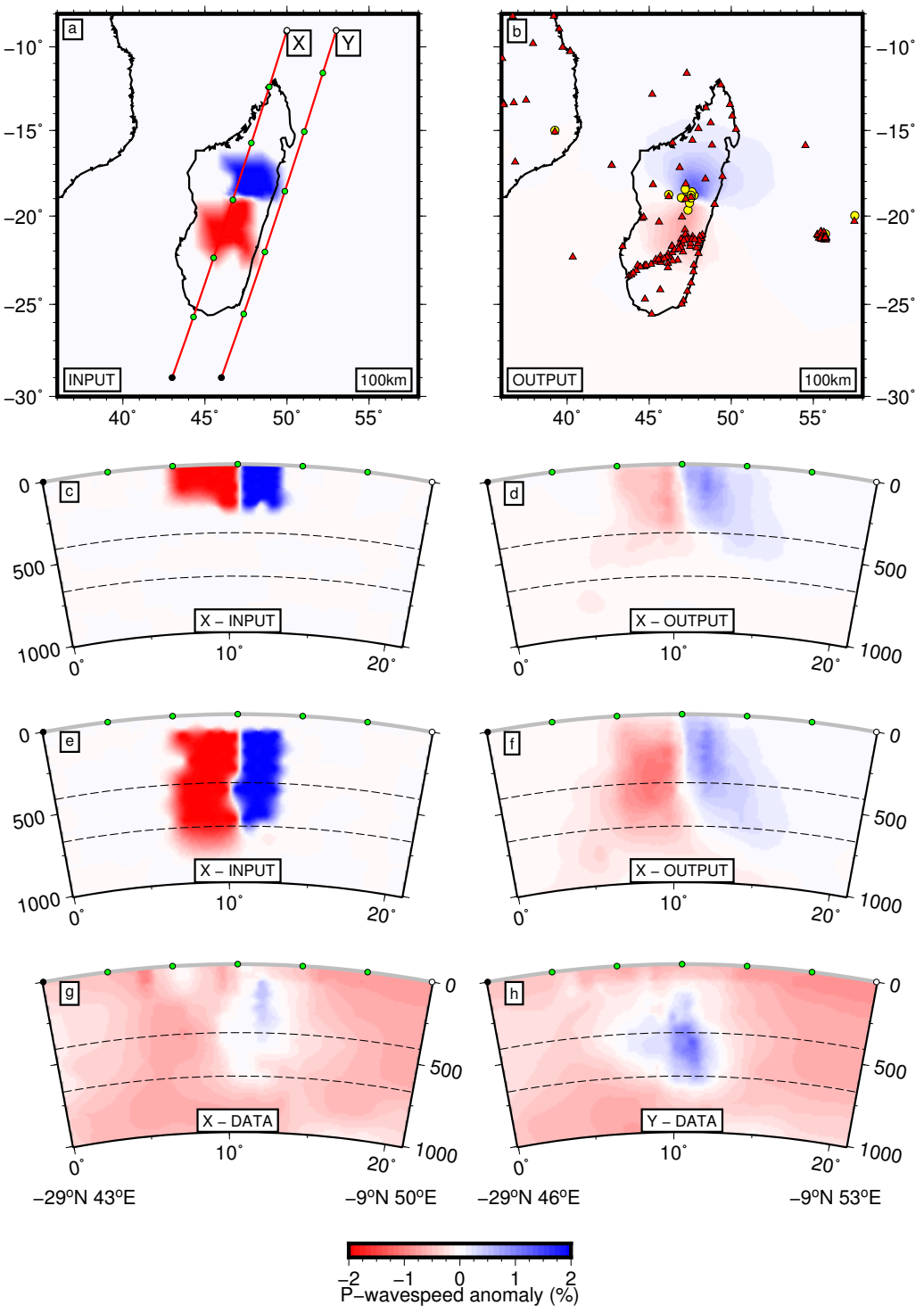

Figure S35. Resolution test for Madagascar using an input (*a,c,e*) rectangular slow wavespeed anomaly of $\delta V_P = -2.0\%$ centered at –20°N, 47°E and rectangular fast wavespeed anomaly of $\delta V_P = +2.0\%$ centered at –17.5°N, 49°E. The depth extent of input anomalies are limited to <250 km in (*c*) and between 100–660 km (*e*). Outputs shown in map (*b*) and cross section "X" (*d,f*) are displayed with the same color scale as the input. The AFRP20 tomographic model (*g,h*) is also shown along the location of cross sections (*X, Y*) marked by the red lines in (*a*). Yellow circles and red triangles on map (*b*) show the locations of "EHB" stations and temporary deployments analyzed in this study (Figures S9, S15).

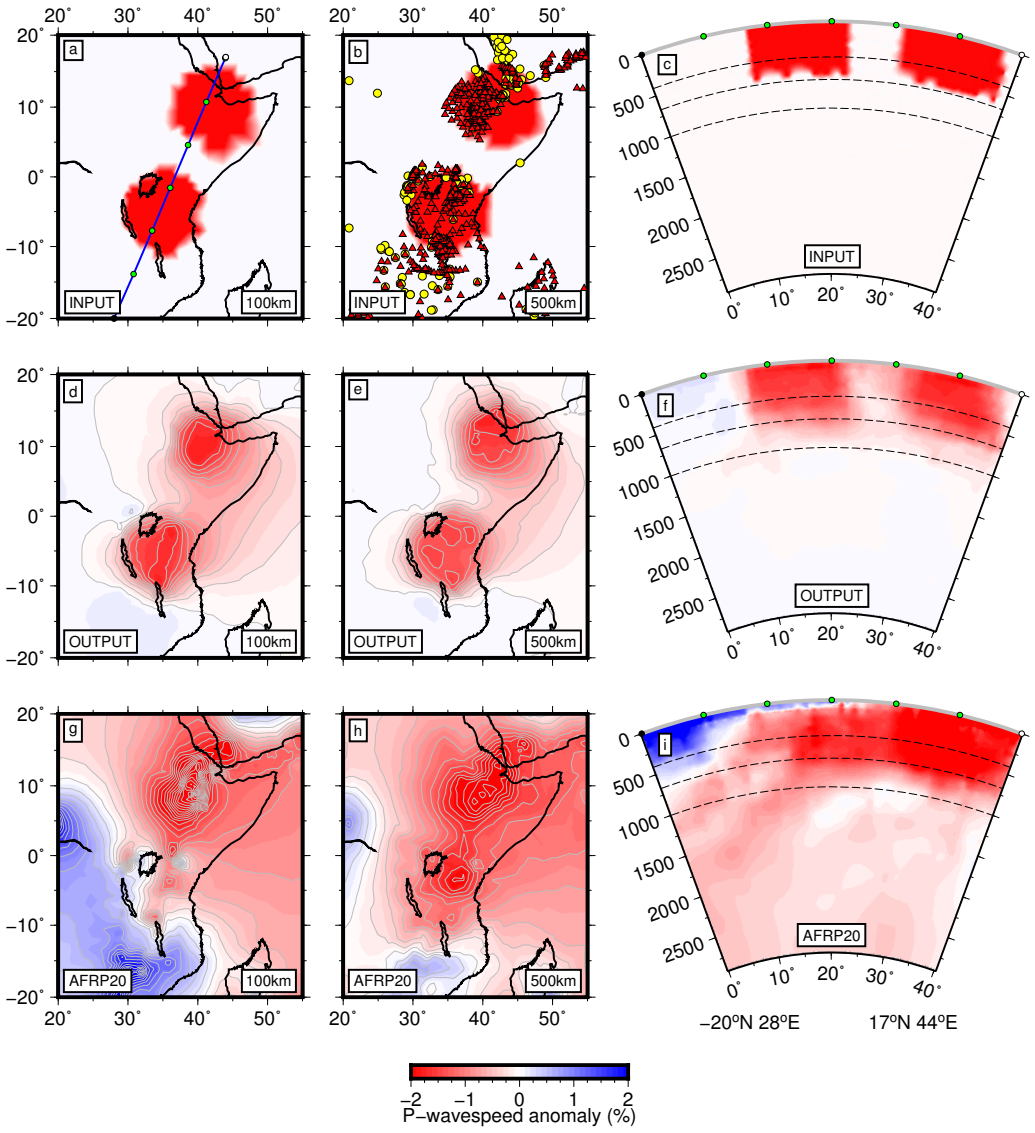

Figure S36. Two elliptical input slow wavespeed anomalies ($\delta V_P = -2.0\%$) extend from the surface to 660 km depth, centered at 10°N, 42°E and at –5°N, 35°E below the Ethiopian and Kenyan plateaus respectively. Visual defects within the input anomaly model result from a coarse adaptive grid in poorly sampled regions - Figure S17. The cross section location used is indicated in (a). Input anomalies (a,b,c) are displayed on the same color scale as the recovered anomalies (d,e,f) and AFRP20 (g,h,i). Yellow circles and red triangles on map (b) show the locations of "EHB" stations and temporary deployments analyzed in this study.

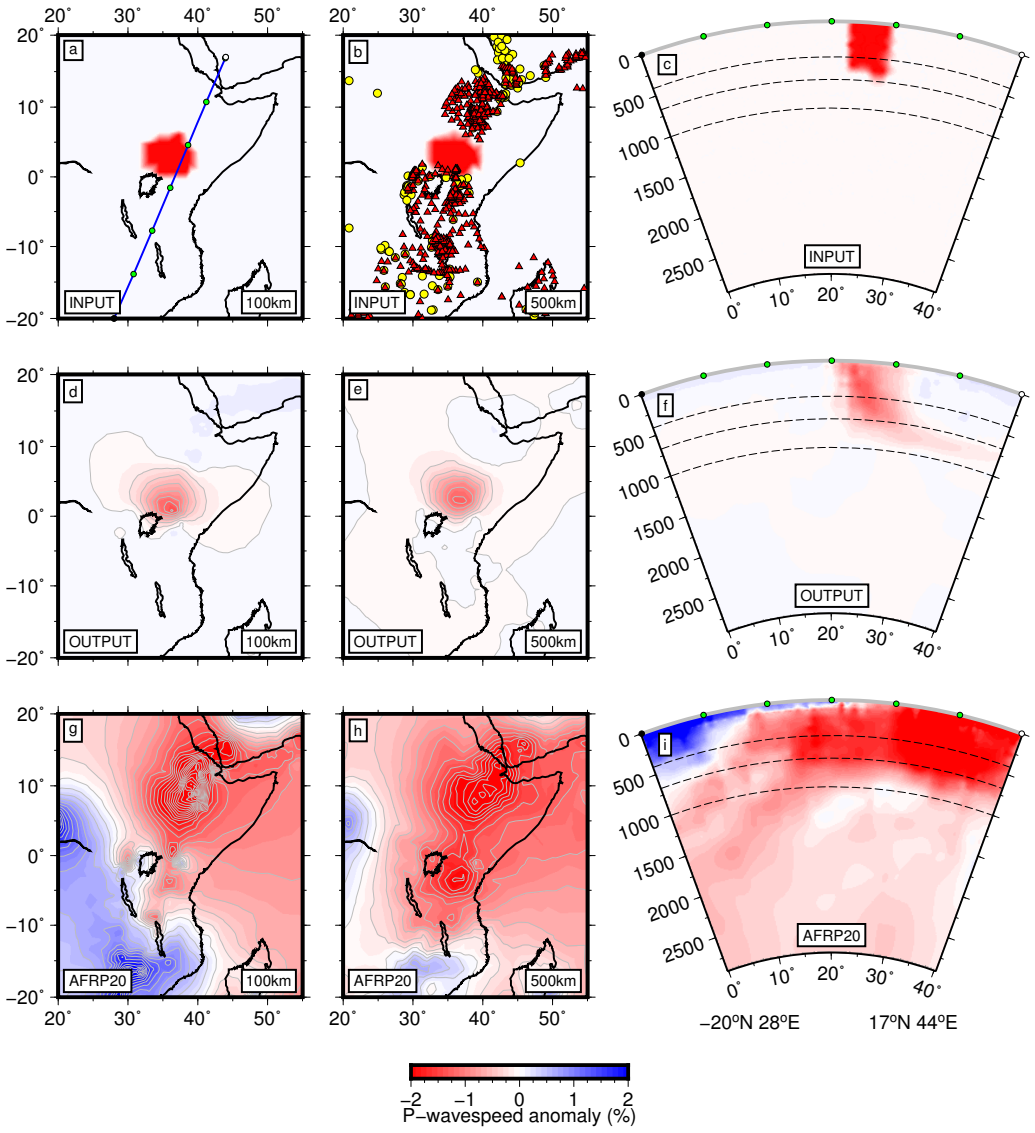

Figure S37. An elliptical input slow wavespeed anomaly ($\delta V_P = -2.0\%$) extends from the surface to 660 km depth, centered at 3°N, 36°E below the Turkana Depression.Visual defects within the input anomaly model result from a coarse adaptive grid in poorly sampled regions - Figure S17. The cross section location used is indicated in (a). Input anomalies (a,b,c) are displayed on the same color scale as the recovered anomalies (d,e,f) and AFRP20 (g,h,i). Yellow circles and red triangles on map (b) show the locations of "EHB" stations and temporary deployments analyzed in this study.

12 Ray Path Masking Technique

Because station distribution is highly variable across Africa we do not expect a somewhat quantitative measure of tomographic resolution, based on checkerboard resolution tests, to be appropriate here (e.g., Boyce et al., 2019). Further it would not be appropriate to make use of the hit count statistics within the parameterized grid since this is accounted for by the adaptive gridding process. Instead we base our tomographic mask entirely on the ray path geometry of the new African temporary network data that is combined with the global data set. We therefore assert that the actual resolving power of the model is much greater than we indicate here since much of the lower mantle will be sufficiently illuminated by the core phases (PKP and PKIKP) included within the global data set. Hence our masking procedure represents a lower bound on model resolving power.

We take all ray paths used to calculate our 87,184 absolute arrival-time residuals and find all pierce points at 50 km depth intervals within the mantle. We only use pierce points less than 80% of the ray turning depth to limit the uncertainty in Fresnel zone shapes caused by horizontally propagating waves. Our data set comprises only direct P-wave measurements so this imposes a theoretical lower depth limit on our ray path mask at ∼2300 km. In practice, since the modal epicentral distance for each data set is ∼60°–85° (Figures S5-S10) the ray path mask is only appropriate for the upper portion of the mantle (<1600 km depth).

Next, we iterate through every pierce point at each depth interval and calculate the distance to each node within a regular "plotting grid" using the haversine formula. Our plotting grid extends from 40°S – 40°N and 20°W – 60°E sampled at 0.25° intervals. We mark a plotting grid node as sampled if one ray passes within one Fresnel zone half width plus the minimum grid cell size within the inversion (∼40 km). We define Fresnel zone half with (FZHW) as the following:

$$FZHW = \sqrt{(\frac{\tau_p V_P}{3} + z)^2 - z^2}, \tag{1}$$

where τ_p defines the natural period of a typical P-wave (taken to be 1 s) and V_P the P-wave wavespeed at the depth z given by ak135 (Kennett et al., 1995).

13 Global P-wave Model Comparison

Figure S38 compares AFRP20 to the global P-wave models PRI-P05 (Montelli et al., 2006), MIT-P08 (Li et al., 2008), LLNL-G3Dv3 (Simmons et al., 2012) and DETOX-P2 (Hosseini et al., 2019) at upper to lower mantle depths.

14 Lower Mantle Sampling

Figure S39 shows globes centered on Afar for each regional data set. Lines show the portion of each ray path that samples the mantle below 2000 km depth, the color indicates the absolute arrival-time residual for the given ray. Stations (green triangles) and earthquakes (yellow circles) are derived from the portion of the data whose epicentral distances are >70°, thus sampling the lower mantle.

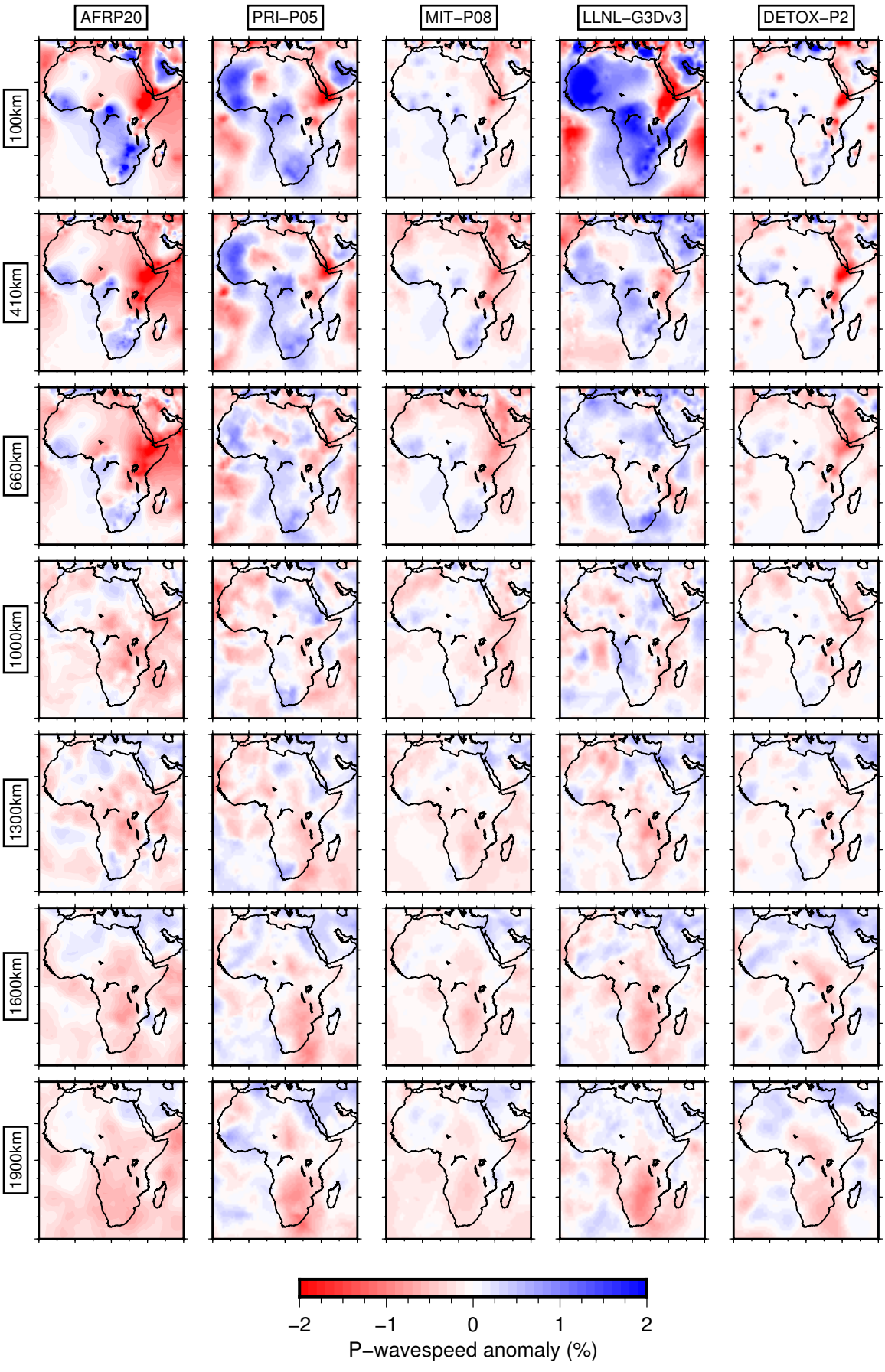
AFRP20
PRI–P05
MIT–P08
LLNL–G3Dv3
DETOX–P2
100km
410km
660km
1000km
1300km
1600km
1900km
–2
–1
0
1
2
P–wavespeed anomaly (%)

Figure S38. Comparison of AFRP20 to other global P-wave models PRI-P05 (Montelli et al., 2006), MIT-P08 (Li et al., 2008), LLNL-G3Dv3 (Simmons et al., 2012) and DETOX-P2 (Hosseini et al., 2019). Wavespeeds are plotted as percentage deviation from the reference model specific to each model. We plot the closest depth slice within each distributed parameterized model.

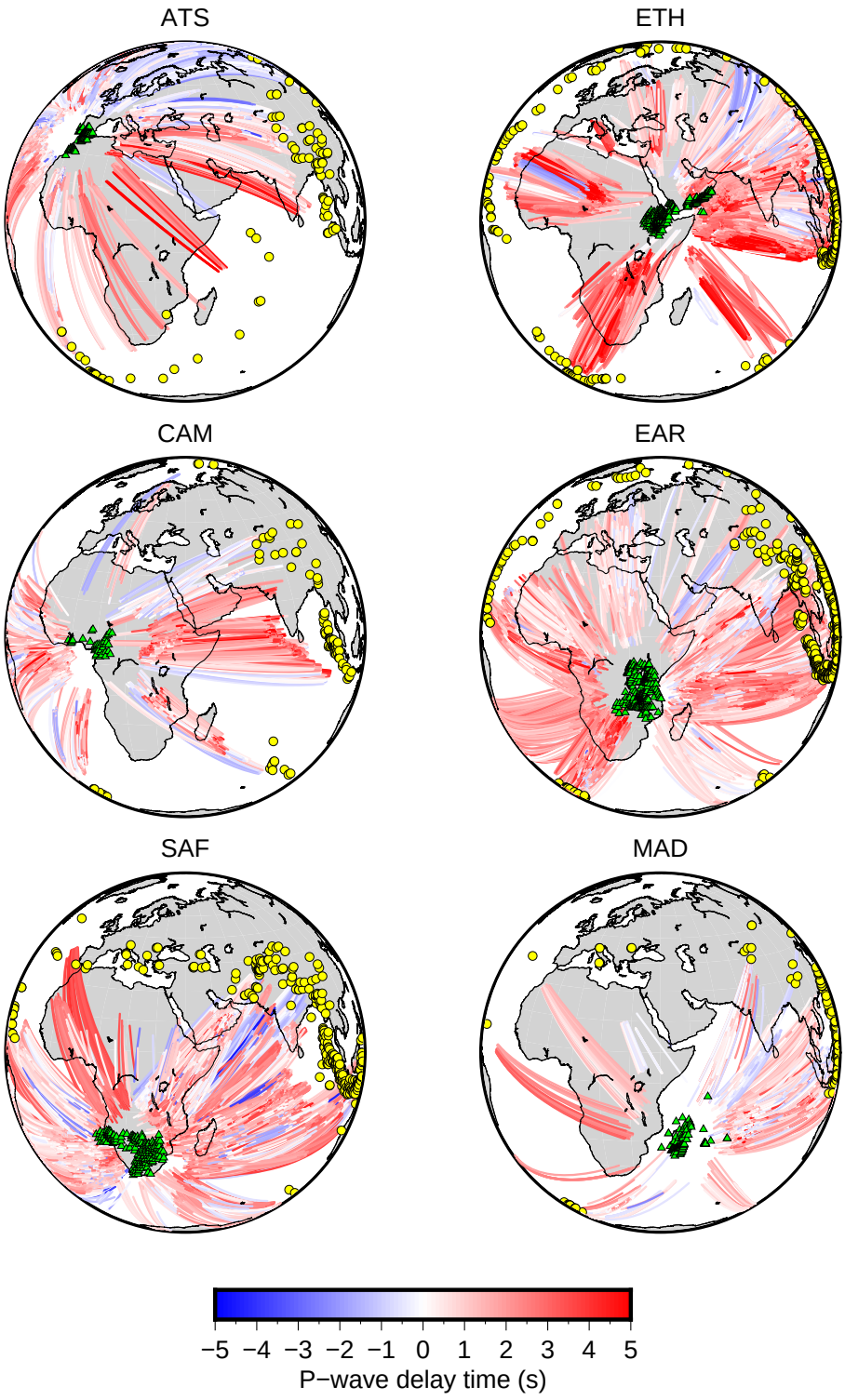

Figure S39. Plot to show the portion of each ray path traveling at depths >2000 km colored by the absolute P-wave delay time for each regional data set. Stations (green triangles) and earthquakes (yellow circles) are plotted for epicentral distances >70°.

15 3-D Model Volume Plots

To highlight low wavespeed anomalies extending into the lower mantle we track the $\delta V_P = -0.5\%$ wavespeed anomaly contour within AFRP20 and display the model volume from multiple perspectives (Figure S40–S43). Here we plot AFRP20 without the crustal correction which causes a static shift to lower wavespeeds in the upper mantle below the oceans, hindering lower mantle visibility.

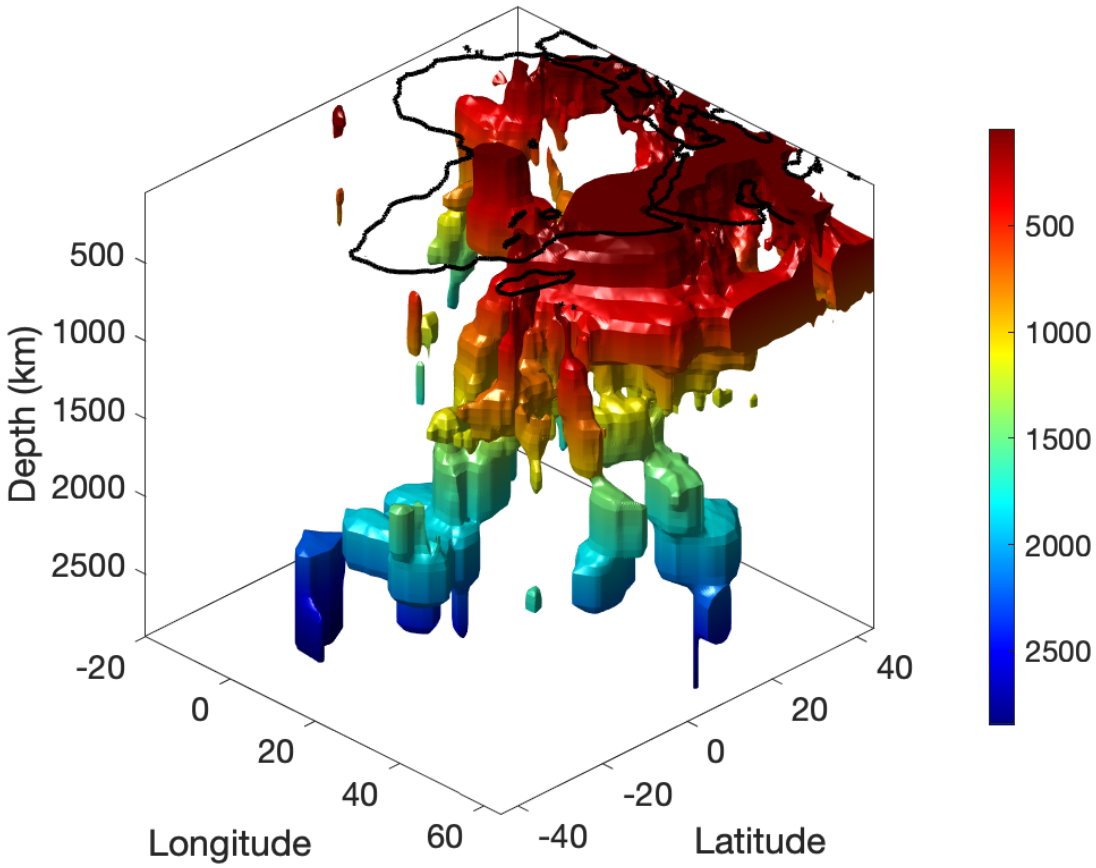

Figure S40. Plot of AFRP20 rendered in 3-D by tracking the $\delta V_P = -0.5\%$ wavespeed anomaly contour within a regularly sampled, lightly smoothed, model grid (50 km in depth, 0.25° horizontally). The African coastline is plotted for reference at 0 km depth. Colors within the model volume represent depth within the mantle. View from the southeast, above ground.

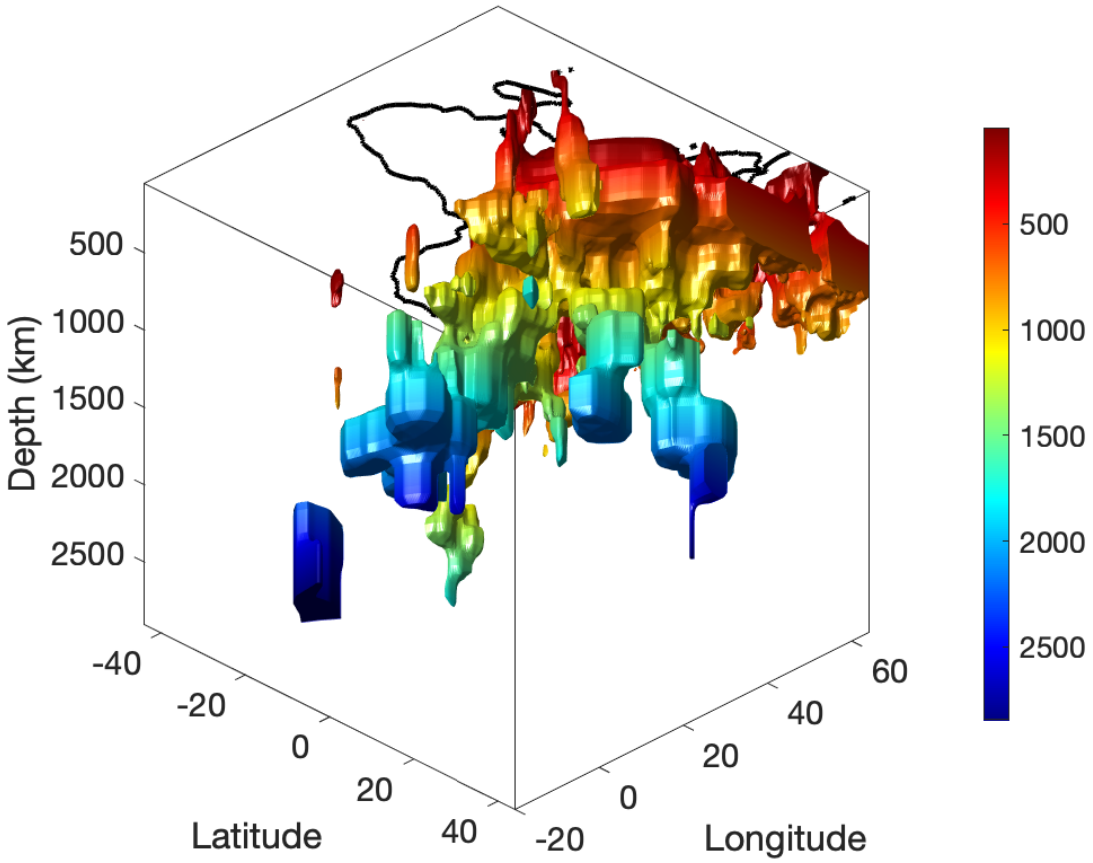

Figure S41. Plot of AFRP20 rendered in 3-D by tracking the $\delta V_P = -0.5\%$ wavespeed anomaly contour within a regularly sampled, lightly smoothed, model grid (50 km in depth, 0.25° horizontally). The African coastline is plotted for reference at 0 km depth. Colors within the model volume represent depth within the mantle. View from the southeast, below ground.

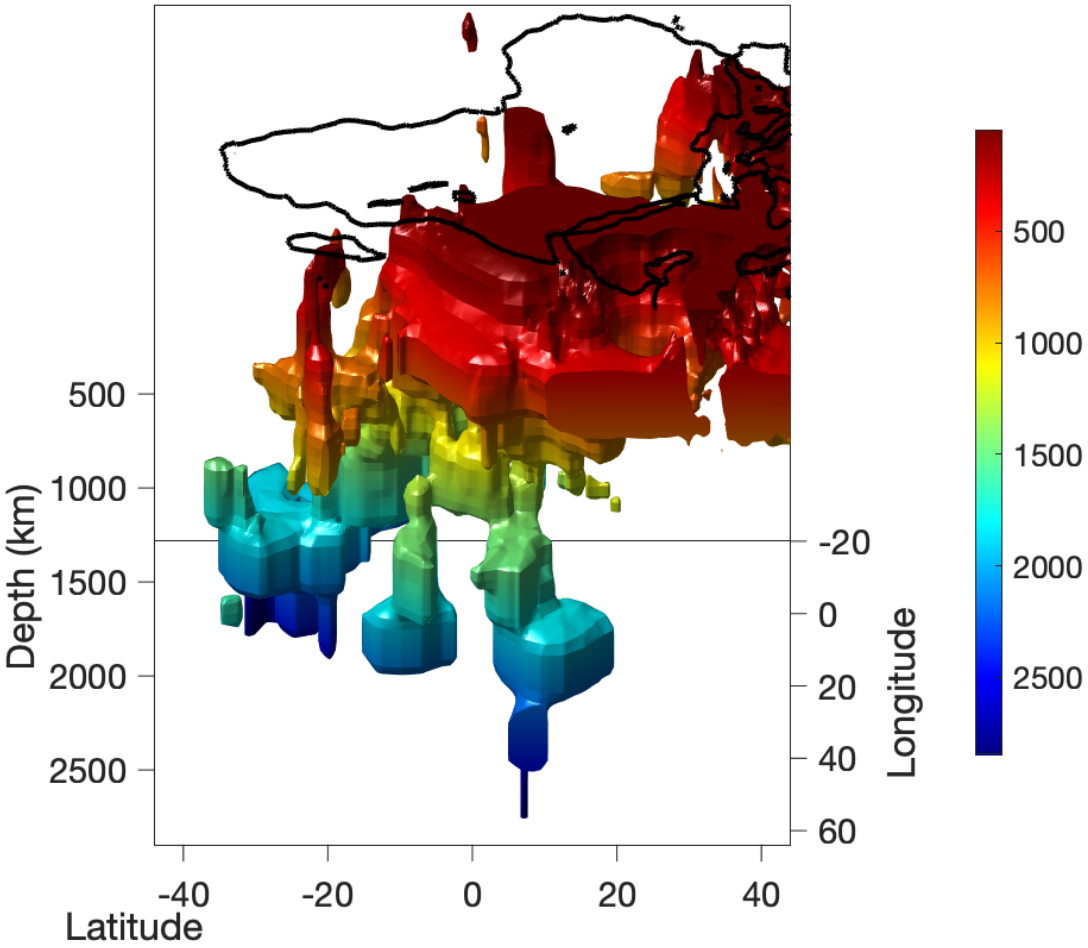

Figure S42. Plot of AFRP20 rendered in 3-D by tracking the $\delta V_P = -0.5\%$ wavespeed anomaly contour within a regularly sampled, lightly smoothed, model grid (50 km in depth, 0.25° horizontally). The African coastline is plotted for reference at 0 km depth. Colors within the model volume represent depth within the mantle. View from the east, above ground.

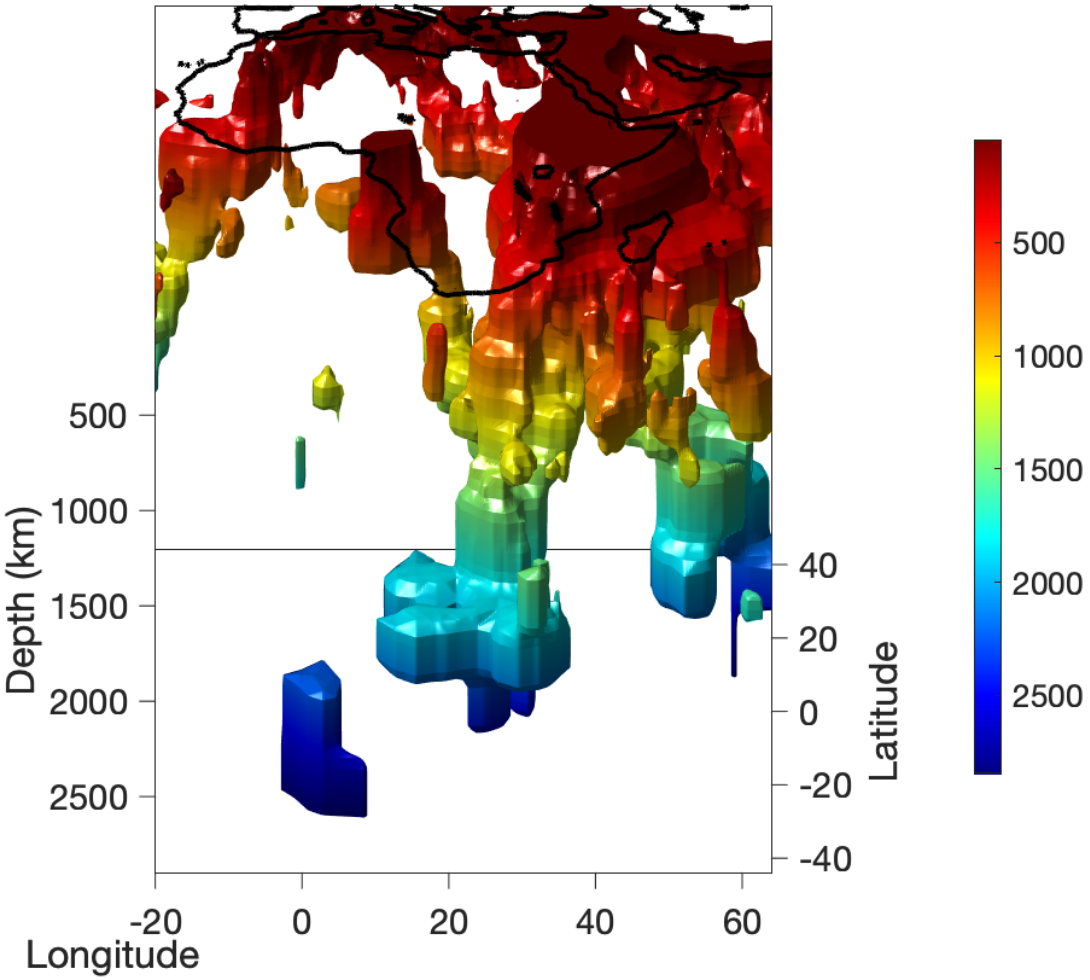

Figure S43. Plot of AFRP20 rendered in 3-D by tracking the $\delta V_P = -0.5\%$ wavespeed anomaly contour within a regularly sampled, lightly smoothed, model grid (50 km in depth, 0.25° horizontally). The African coastline is plotted for reference at 0 km depth. Colors within the model volume represent depth within the mantle. View from the south, above ground.

References

Akpan, O., Nyblade, A. A., Okereke, C., Oden, M., Emry, E., & Julià, J. (2016). Crustal structure of Nigeria and Southern Ghana, West Africa from P-wave receiver functions. *Tectonophysics*, *676*, 250–260. doi: 10.1016/j.tecto.2016.02.005

Andriampenomanana, F., Nyblade, A. A., Wysession, M. E., Durrheim, R. J., Tilmann, F., Julià, J., ... Rakotondraibe, T. (2017). The structure of the crust and uppermost mantle beneath Madagascar. *Geophys. J. Int.*, *210*(3), 1525–1544. doi: 10.1093/gji/ggx243

Boyce, A., Bastow, I. D., Darbyshire, F. A., Ellwood, A. G., Gilligan, A., Levin, V., & Menke, W. (2016). Subduction beneath Laurentia modified the eastern North American cratonic edge: Evidence from P wave and S wave tomography. *J. Geophys. Res.*, *121*(7), 5013–5030. doi: 10.1002/2016JB012838

Boyce, A., Bastow, I. D., Golos, E. M., Rondenay, S., Burdick, S., & Van der Hilst, R. D. (2019). Variable modification of continental lithosphere during the Proterozoic Grenville orogeny: Evidence from teleseismic P-wave tomography. *Earth Planet. Sci. Lett.*, *525*, 115763. doi: 10.1016/j.epsl.2019.115763

Boyce, A., Bastow, I. D., Rondenay, S., & Van der Hilst, R. D. (2017). From relative to absolute teleseismic travel-times: the Absolute Arrival-time Recovery Method (AARM). *Bull. Seis. Soc. Am.*, *107*(5), 2511—2520. doi: 10.1785/0120170021

Burdick, S., Vernon, F. L., Martynov, V., Eakins, J., Cox, T., Tytell, J., ... Van der Hilst, R. D. (2017). Model Update May 2016: Upper-Mantle Heterogeneity beneath North America from Travel-Time Tomography with Global and USArray Data. *Seis. Res. Lett.*, *88*(2A), 319–325. doi: 10.1785/0220160186

Ebinger, C. J., Keir, D., Bastow, I. D., Whaler, K., Hammond, J. O. S., Ayele, A., ... Hautot, S. (2017). Crustal Structure of Active Deformation Zones in Africa: Implications for Global Crustal Processes. *Tectonics*, *36*(12), 3298–3332. doi: 10.1002/2017tc004526

Engdahl, E. R., Van der Hilst, R. D., & Buland, R. (1998). Global teleseismic earthquake relocation with improved travel times and procedures for depth determination. *Bull. Seis. Soc. Am.*, *88*(3), 722–743.

Fadel, I., Meijde, M., & Paulssen, H. (2018). Crustal Structure and Dynamics of Botswana. *J. Geophys. Res.*, *123*(12), 10,659–10,671. doi: 10.1029/2018jb016190

Hosny, A., & Nyblade, A. A. (2016). The crustal structure of Egypt and the northern Red Sea region. *Tectonophysics*, *687*, 257–267. doi: 10.1016/j.tecto.2016.06.003

Hosseini, K., Sigloch, K., Tsekhmistrenko, M., Zaheri, A., Nissen-Meyer, T., & Igel, H. (2019). Global mantle structure from multifrequency tomography using P, PP and P-diffracted waves. *Geophys. J. Int.*, *220*(1), 96–141. doi: 10.1093/gji/ggz394

Kennett, B. L. N., Engdahl, E. R., & Buland, R. (1995). Constraints on seismic velocities in the earth from traveltimes. *Geophys. J. Int.*, *122*(1), 108-124. doi: 10.1111/j.1365-246X.1995.tb03540.x

Laske, G., Masters., G., Ma, Z., & Pasyanos, M. E. (2013). Update on CRUST1.0 - A 1-degree Global Model of Earth's Crust. In *Geophys. res. abstracts, 15, abstract egu2013-2658* (p. EGU2013-2658).

Lemnifi, A. A., Elshaafi, A., Browning, J., Aouad, N. S., El Ebaidi, S. K., Liu, K. K., & Gudmundsson, A. (2017). Crustal Thickness Beneath Libya and the Origin of Partial Melt Beneath AS Sawda Volcanic Province From Receiver Function Constraints. *J. Geophys. Res.*, *122*(12), 10,037–10,051. doi: 10.1002/2017jb014291

Li, C., Van der Hilst, R. D., Engdahl, R., & Burdick, S. (2008). A new global model for P wave speed variations in Earth's mantle. *Geochem. Geophys. Geosyst.*,

9(5). doi: 10.1029/2007GC001806

Montelli, R., Nolet, G., Dahlen, F., & Masters, G. (2006). A catalogue of deep mantle plumes: new results from finite-frequency tomography. *Geochem. Geophys. Geosyst.*, *7*, Q11007. doi: 10.1029/2006GC001248

Ogden, C. S., Bastow, I. D., Gilligan, A., & Rondenay, S. (2019). A reappraisal of the H–κ stacking technique: implications for global crustal structure. *Geophys. J. Int.*, *219*(3), 1491–1513. doi: 10.1093/gji/ggz364

Simmons, N. A., Myers, S. C., Johannesson, G., & Matzel, E. (2012). LLNL-G3Dv3: Global P wave tomography model for improved regional and teleseismic travel time prediction. *J. Geophys. Res.*, *117*(B10). doi: 10.1029/2012jb009525

VanDecar, J., & Crosson, R. (1990). Determination of teleseismic relative phase arrival times using multi-channel cross-correlation and least squares. *Bull. Seis. Soc. Am.*, *80*(1), 150-169.